MEMS FOURIER TRANSFORM SPECTROMETER USING LAMELLAR GRATING

by

Hüseyin Rahmi Seren

A Thesis Submitted to the
Graduate School of Engineering
in Partial Fulfillment of the Requirements for
the Degree of

Master of Science

in

Electrical & Computer Engineering

Koc University

August, 2009

Koç University

Graduate School of Sciences and Engineering

This is to certify that I have examined this copy of a master's thesis by

Hüseyin Rahmi Seren

and have found that it is complete and satisfactory in all respects,
and that any and all revisions required by the final
examining committee have been made.

Committee Members:

_____

Hakan Ürey, Ph. D. (Advisor)

_____

Erdem Alaca, Ph. D.

_____

Arda D. Yalçınkaya, Ph. D.

Date: _____

ABSTRACT

Fourier Transform Infrared (FTIR) Spectroscopy is a widely used method for chemical and/or biological substance analysis and identification. FTIR uses a single photodetector instead of an array of detectors and offers several advantages over the other spectroscopy methods such as high signal to noise ratio, high throughput, compact form-factor, and low-cost. Currently the FTIR spectrometers are mostly bulky and mechanically sensitive instruments which can be used under laboratory conditions by trained persons. However, there is a great need for portable instruments in various industrial fields.

In this thesis, a lamellar grating interferometer (LGI) device using Micro-Electro-Mechanical-Systems (MEMS) technology is developed as a part of an 7th framework project MEMFIS funded by EU, which aims at developing an ultra-small FTIR spectrometer system. The mechanical, optical, and electro-mechanical properties of the device are optimized and significantly improved compared to the state-of-the art in this area. Theoretical limits of the LGI are established using Fourier optics theory, and diffraction grating shape and period are optimized as part of the optical system design and optimization study. Numerical analyses are made to optimize optical efficiency of the device for the mid-wavelength infrared (2.5 μm – 16 μm). To improve the mechanical design, pantograph-type spring suspensions are designed using ANSYS™ finite element modeling tool to increase the translational amplitude of the device to ±500 μm and to improve shock and vibration survivability. Thus, the theoretical spectral resolution limit is enhanced to 10 cm^{-1}, which should provide a 10-fold increase over the previous generation MEMS FTS system demonstrated at Koç University. Negative effects of the dynamic deformation of the grating reflectors on the spectral resolution are eliminated by limiting it to 300 nm by decoupling the mechanical springs from the diffraction gratings. Electro-mechanical properties of the nonlinear actuator are analyzed in detail and the expected full-

performance should be achievable with <200V of actuation voltage and without using a vacuum package.

ÖZET

Fourier Dönüşümü Kızılötesi (FTIR) Spektroskopi kimyasal ve/veya biyolojik maddelerin tanımlanması ve analizinde çokça kullanılan bir yöntemdir. Bu yöntemde tüm ışık bir foto detektörün üstünde toplandığından diğer yöntemlere kıyasla birçok avantajı vardır. Bunlara örnek olarak yüksek işaret-gürültü oranı ve ölçüm hızı, küçültülebilir ve ucuzlatılabilir olması verilebilir. Mevcut FTIR spektrometreler çoğunlukla eğitimli personel tarafından kullanılabilen, büyük ve hassas cihazlardır. Diğer taraftan, değişik endüstrilerde, sahada kullanılmak üzere bu cihazlara büyük ihtiyaç duyulmaktadır. Bu ihtiyaç, FTIR spektrometrelerin küçültülmesi ve dayanıklılaştırılması gereğini doğurur.

Bu tezde, 7inci çerçeve projesi olan Avrupa Komisyonu tarafından desteklenen MEMFIS kapsamında, Mikro-Elektro-Mekanik-Sistemler (MEMS) teknolojisi kullanılarak Kırınım Izgaralı Girişimölçerli (LGI) FTIR spektrometreler için bir MEMS cihazı geliştirilmiştir. Cihazın optik, mekanik ve elektromekanik özellikleri eniyileştirilmiş ve mevcut benzerlerine göre önemli ölçüde geliştirilmiştir. Kırınım ızgarası yönteminin teorik limitleri Fourier optiği prensipleri kullanılarak ortaya konmuş ve optik sistem tasarımı ve eniyileştirilmesi kapsamında ızgara şekil ve periyodu tasarlanmıştır. Cihazın optik verimliliği yapılan sayısal analizlerle orta dalga kızılötesinde (2.5μm – 16μm) çalışacak şekilde geliştirilmiştir. Cihazın düzlem dışı hareketi ANSYS^{TM} sonlu elementler modelleme programı kullanılarak tasarlanan pantograf tipi yapılarla sağlanarak, hareket genliği ±500 μm'ye çıkarılmış; aynı zamanda darbe ve sarsıntıya dayanırlılığı artırılmıştır. Böylelikle teorik spektral çözünürlük 10 cm-1'e kadar iyileştirilmiştir. Buna göre daha önce Koç Üniversitesi'nde geliştirilen MEMS cihaza göre 10 kat daha iyi bir performans beklenmektedir. Yansıtıcı ızgaralardaki dinamik deformasyon yardımcı süspansiyon mekanizmayla 300nm'ye düşürülerek çözünürlük üstündeki olumsuz etkileri yok edilmiştir. Doğrusal olmayan elektromekanik sürme sistemi detaylı olarak analiz edilmiştir

ve istenen performansın 200V'tan düşük giriş voltajıyla vakum paketine gerek olmadan elde edilebileceği gösterilmiştir.

ACKNOWLEDGEMENTS

I would like to express my gratitude to my thesis advisor, Prof. Hakan Ürey. He gave me the chance to participate in the laboratory projects as an active member starting when I was a junior student and now I graduate as a Master student. I gain my all experience and expertise thanks to his research and working understanding and his belief to me. I thank him for building the fundamentals of my academic career. I also thank Prof. Erdem Alaca and Prof. Arda D. Yalçınkaya for taking place in my thesis committee and for their precious contributions.

MEMFIS project is a large team work and I would like to thank all of the MEMFIS partners and especially Thilo Sandner, Thomas Grasshoff and Stefan Menzel from Fraunhofer IPMS, Arno Simon and Stephan Lüttjohann from Bruker Optics, and Jean-Louis Stehle from Sopralab. Their critics and guidance were very helpful and beneficial for the maturation of this work.

I gratefully acknowledge TÜBİTAK BIDEB for scholarship for graduate study. I thank TUBITAK and Koç University for paving the way of research environment with their support and increasing the quality and importance of academic works.

Working hard would not be possible without such joyful laboratory members. They are all good friends and colleagues. Plus, I thank Çağlar Ataman, Onur Ferhanoğlu, Gökhan Hatipoğlu, Kishore Chellappan, Erdem Erden, and Selim Ölçer for their essential contributions in this thesis. I thank Kutal Gökçe and Sven Holmström for their hard and patient work for the fabrication. I would like to thank Aslıhan Arslan for being good research, travel, and cinema fellows and being a real friend to me. I also thank Engin, Can and Ersen for the nice home environment.

Finally, nothing would be possible for me without my family. Anne, Baba, Abi, Abla, I am grateful to you for always keeping your endless love, support, and trust.

TABLE OF CONTENTS

LIST OF TABLES

LIST OF FIGURES

NOMENCLATURE

FEM	Finite Element Modeling
FTIR	Fourier Transform Infra-Red (Spectroscopy)
FTS	Fourier Transform Spectroscopy
FWHM	Full Width at Half Maximum
IPMS	Institute for Photonic Microsystems
IR	Infrared
LGI	Lamellar Grating Interferometer
M(O)EMS	Micro-(Opto)-Electro-Mechanical Systems
NA	Numerical Aperture
N/M/F/IR	Near/Mid/Far Infra-Red
OPD	Optical Path Difference
k	Wavenumber
λ	Wavelength
Λ	Grating Period

Chapter 1

1 INTRODUCTION

Infrared (IR) Spectroscopy is a very commonly used and well known analytical method which is utilized for matter identification and characterization without damaging the sample. The fundamental working principle of IR spectroscopy is explained by the atomic and/or molecular vibration and rotation modes. These modes have specific energy levels and resonance frequencies. Most of the molecular resonance frequencies are concentrated between 4000 cm^{-1} and 50 cm^{-1}. Those frequencies correspond to 2.5 μm - 200 μm wavelength range in electromagnetic waves which is called as the infrared spectra. When a molecule is exposed to an electromagnetic radiation which has enough power and the same frequency as the molecule's vibrational/rotational modes, the radiation energy is absorbed and the energy level of the molecule changes. Due to different molecular properties, each substance has different absorption band. Therefore, if the absorption bands of a specific material are known, the material can be identified using infrared spectroscopy techniques [1]-[3].

1.1 Fourier Transform Spectroscopy

There are several methods developed for spectroscopy such as transmission, reflectance, dispersive, or photo-acoustic spectroscopy [4]. After the development of Fourier Transform Spectroscopy (FTS), however, it is dominantly used because of its higher performance. Fourier Transform Spectrum is obtained using the interferogram which is change in the intensity of a self-interfering beam with respect to optical path

length difference between the interfering arms. Hence, given the intensity variation at known optical path length differences, the spectrum of light can be retrieved by a Fourier Transformation. (1.1) shows the Fourier transform relation between spectrum (*S*), and the intensity (*I*), which is a function of optical path length difference between interfering beams (*x*), and the wave number (*k*).

$$S(k) = \int_{0}^{x_{amp}} I(x) e^{-jkx} dx \tag{1.1}$$

FTIR spectrometry has certain advantages over the other methods. Single detector configuration has a significant contribution in saving the light budget and increasing the signal to noise ratio (SNR). These advantages are known as throughput or Jacquinot advantage and multiplex or Felgett advantage [5]. Having a stable wavelength laser interferometry for the data sampling, FTIR also provide high accuracy in measurement. On the other hand, the need for light source stability, sensitive optical alignment, and the complex post-processing can be counted among the disadvantages of the technique.

1.1.1 Michelson type FTIR spectrometer

The most commonly used FTIR spectroscopy conformation is based on Michelson interferometry (Figure 1.1). In this conformation, the IR light is split into two arms with the help of a beam splitter. This is called as amplitude division. The light in the two arms are reflected back from the mirrors where one is stationary and the other one is moving. Moving mirror changes the optical path length traveled by the light. Reflected light beams interfere and the interference intensity change according to optical path length difference. The intensity change is recorded through a photo detector. This time varying intensity change is called as *interferogram*. Interferogram has whole wavelength content information in it and this information can be more evident after Fourier transformation. However, the

record, itself, cannot give the relation between optical path length difference and the intensity change.

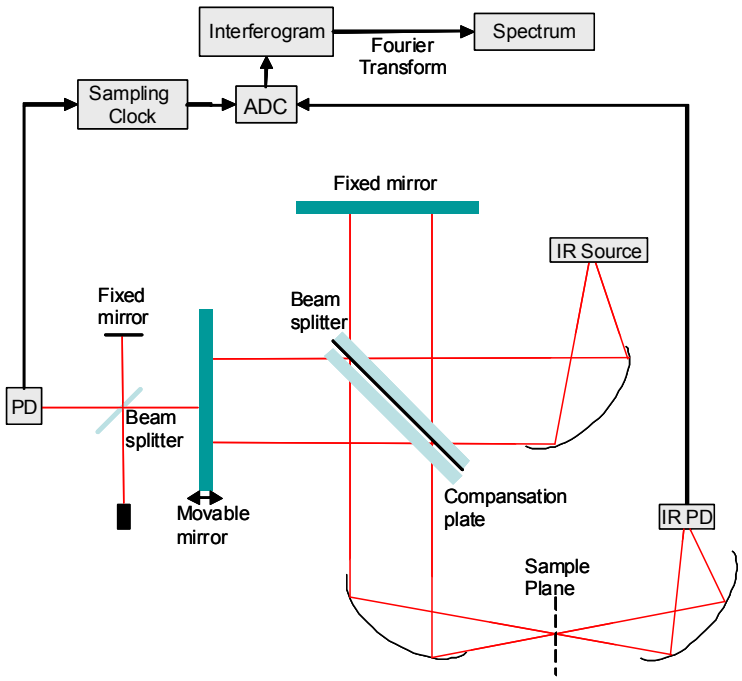

Figure 1.1 - Michelson type spectrometer layout

For this purpose the position of the moving mirror should be determined at each recording instances. A well known method for the position feedback is the reference laser interferometry. Another Michelson interferometry setup is established that uses the same moving mirror as the IR spectrometer. In this additional setup, a laser beam whose wavelength is stable and precisely known is used. Then, the reference interferogram is recorded simultaneously with the IR interferogram. Using the reference interferogram the optical path length differences can be computed since the wavelength is fixed and known. IR interferogram is converted from analog to digital signal by taking samples based on the reference interferogram. The sampling should be made at equal distance changes. As the

last step the Fourier Transformation is applied using an appropriate apodization window which reveals the *spectrum* of IR light. If the light passed through a substance before the collection on the photo detector, the absorption bands of the substance can be detected by comparing it with the measurement without any substances.

1.1.2 Lamellar grating type FTIR spectrometer

Lamellar Grating Interferometry (LGI) is first introduced by Strong and Vanessa in the late 1950's [6] (Figure 1.2). The preliminary lamellar gratings were designed mostly to be operated in far infrared region, i.e. below 100 cm^{-1}, and proved to be more efficient than conventional Michelson configuration. This limitation for the operation region arose because of the machining limitations. On the other hand, with the current Micro-Electro-Mechanical-Systems (MEMS) technology, LGI can be available even for visible band.

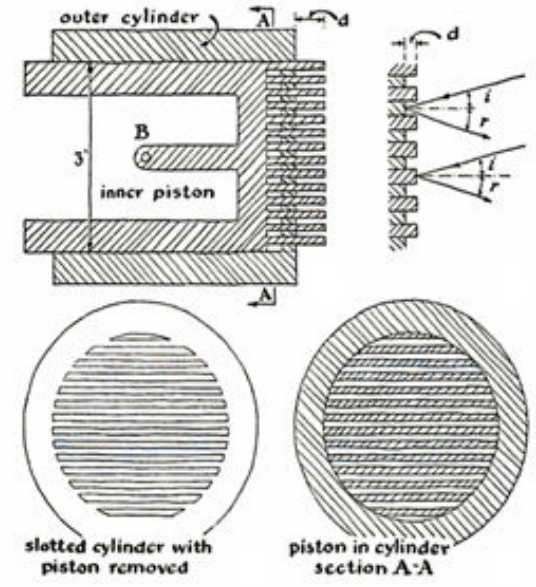

Figure 1.2 - One of the first LGI prototypes by Strong and McCubbin [7]

Different from Michelson interferometry, LGI uses wavefront division which removes the necessity of the beam splitter and the stationary mirror, and relaxes the alignment tolerances. One portion of the wave reflects from the stationary grating strips while the remaining reflects from the moving strips as it can be interpreted from Figure 1.3. Because of the moving part, an optical path length difference occurs between the reflected waves. The full interference of these reflected waves can be observed at a distance, i.e. *Fraunhofer distance,* away from the grating. Varying the path length difference, an interferogram can be recorded at the zeroth order of the far field diffraction pattern, which is essential for FTS.

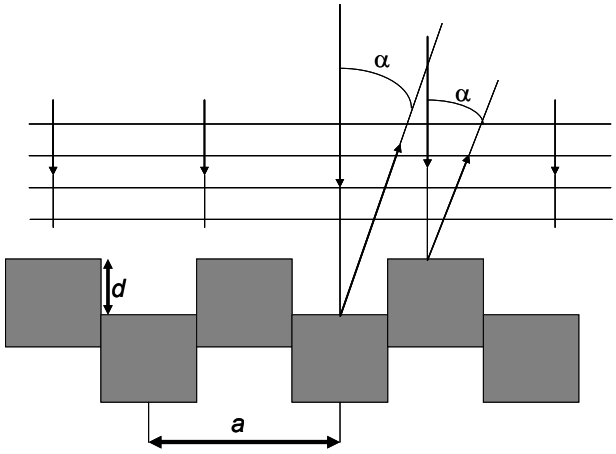

Figure 1.3 - Grating fingers with d mechanical path length difference and a plane wave at normal incidence

Assuming large feature size of the grating structure with comparison to the interested wavelengths, scalar diffraction theory can be utilized to show how an interferogram can be acquired at the zeroth order of the Fraunhofer field pattern. This analysis is given in detail in [8] as follows for normal incident monochromatic plane wave with wavelength λ:

$$E_{front} = EF \tag{1.2}$$

where E_{front} is the diffracted electric field at the far field reflected from the front facets, E is the diffracted wave amplitude and F is the interference term caused by the front grating fingers (note that fingers and facets are used interchangeably). For a grating of period Λ, expected electric field amplitude for diffracted wave at angle α is proportional to

$$E \propto \frac{\sin\left(\pi\Lambda\sin(\alpha)/2\lambda\right)}{\pi\Lambda\sin(\alpha)/2\lambda} \tag{1.3}$$

and the interference term for N fingers of the same grating is

$$F \propto \frac{\sin\left(N\pi\Lambda\sin(\alpha)/\lambda\right)}{\sin\left(\pi\Lambda\sin(\alpha)/\lambda\right)}\exp\left(-j\frac{(N-1)\pi\Lambda\sin(\alpha)}{\lambda}\right) \tag{1.4}$$

The reflection from the back grating can also be expressed in the same manner but only adding the phase difference ϕ caused by the optical path length difference:

$$E_{back} = EFe^{j\phi} \tag{1.5}$$

where ϕ is

$$\phi = \frac{2\pi d}{\lambda}\left[(1+\cos(\alpha)) + (\Lambda/2d)\sin(\alpha)\right] \tag{1.6}$$

Total electric field becomes the sum of the two fields and intensity at the far field is the magnitude square of the diffracted electric field.

$$E_{total} = E_{front} + E_{back} \tag{1.7}$$

$$I \propto EE^{*}$$
$$\propto \left\{ \frac{\sin\left(\pi \Lambda \sin(\alpha) / 2\lambda \right)}{\pi \Lambda \sin(\alpha) / 2\lambda} \right\}^{2} \left\{ \frac{\sin\left(N\pi \Lambda \sin(\alpha) / \lambda \right)}{\sin\left(\pi \Lambda \sin(\alpha) / \lambda \right)} \right\}^{2} \cos^{2}\left(\frac{\phi}{2} \right) \tag{1.8}$$

Equation (1.8) can be examined in three parts. The first part determines the envelope of the pattern which is the square of a sinc function. This is basically determined by the grating shape and period, and the wavelength (Figure 1.4).

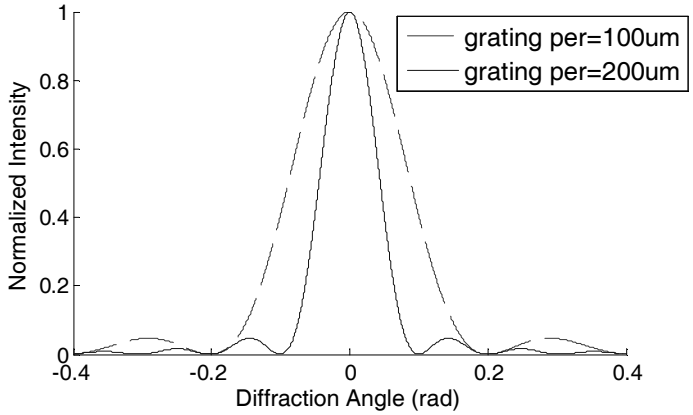

Figure 1.4 - Far field intensity envelope that is determined by the wavelength, grating period, and the shape of the grating structure. The plot shows envelopes for two different grating periods with 50% duty-cycle square shape and 10 µm wavelength.

The second part resembles a pulse train and shows the interference pattern. The pulse positions correspond to high intensity variation spots which are called as *orders*. This part of the equation reaches its maximum, which is N^2, when insides of the sines become zero. Therefore, order positions can be determined as

$$\pi \Lambda \sin(\alpha) / \lambda = m\pi$$
$$\alpha = \sin^{-1}\left(m \frac{\lambda}{\Lambda} \right) \tag{1.9}$$

where *m* is called as order number. As the number of illuminated periods, i.e. *N*, increases, the pulses, or orders, become narrower (Figure 1.5). In lamellar grating configuration even orders other than 0^{th} order does not appear because the first term in (1.8) becomes always zero for even values of *m* (Figure 1.6).

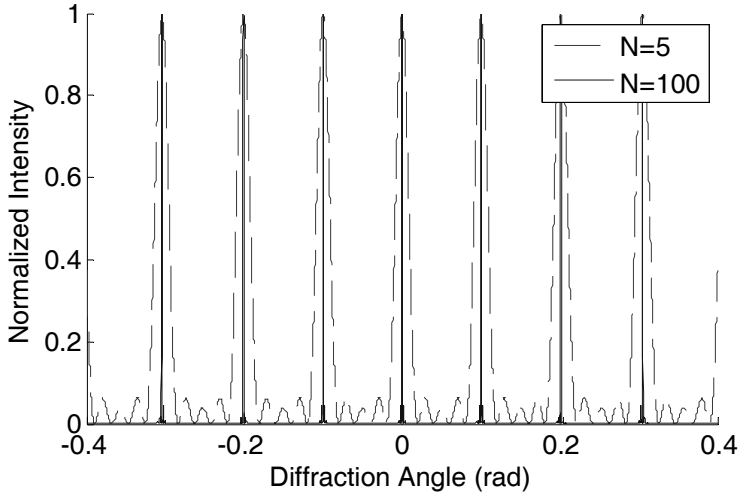

Figure 1.5 – Pulse train that is imposed by the second term of (1.8). The effect of number of illuminated periods is shown. Both even and odd orders are present.

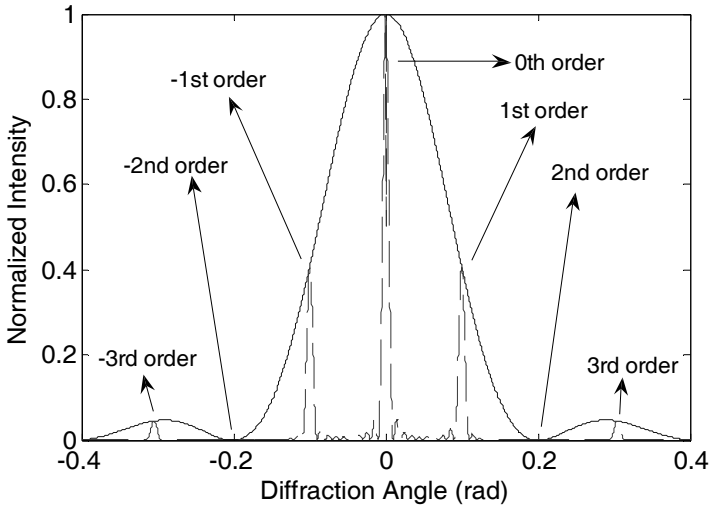

Figure 1.6 – Multiplication of the first two terms of (1.8): Even orders except 0^{th} order disappear.

The last part brings the optical path length difference dependence, which is the phase difference between the interfering waves. Phase difference shows a diffraction angle dependent variation. This variation results in $\pi/2$ phase difference between the intensity modulation at 0^{th} and higher orders (Figure 1.7).

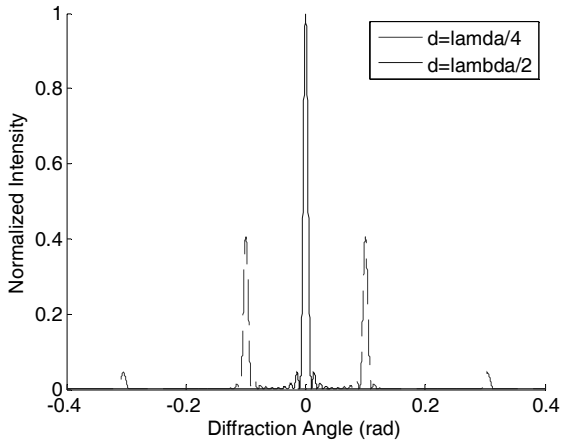

Figure 1.7 – Constructive and destructive interferences at 0^{th} and higher orders occur out of phase (d shows the mechanical displacement)

As can be inferred from Figure 1.7, 1st order intensity amplitudes can reach at most about 40% of the 0th order. Moreover, 0th order location is wavelength independent while higher order positions change. Therefore 0th order of the diffraction pattern intensity can be recorded for an interferogram acquisition. Rest of the procedure follows the same path as in Michelson type spectrometers. An example LGI type spectrometer layout is illustrated in Figure 1.8.

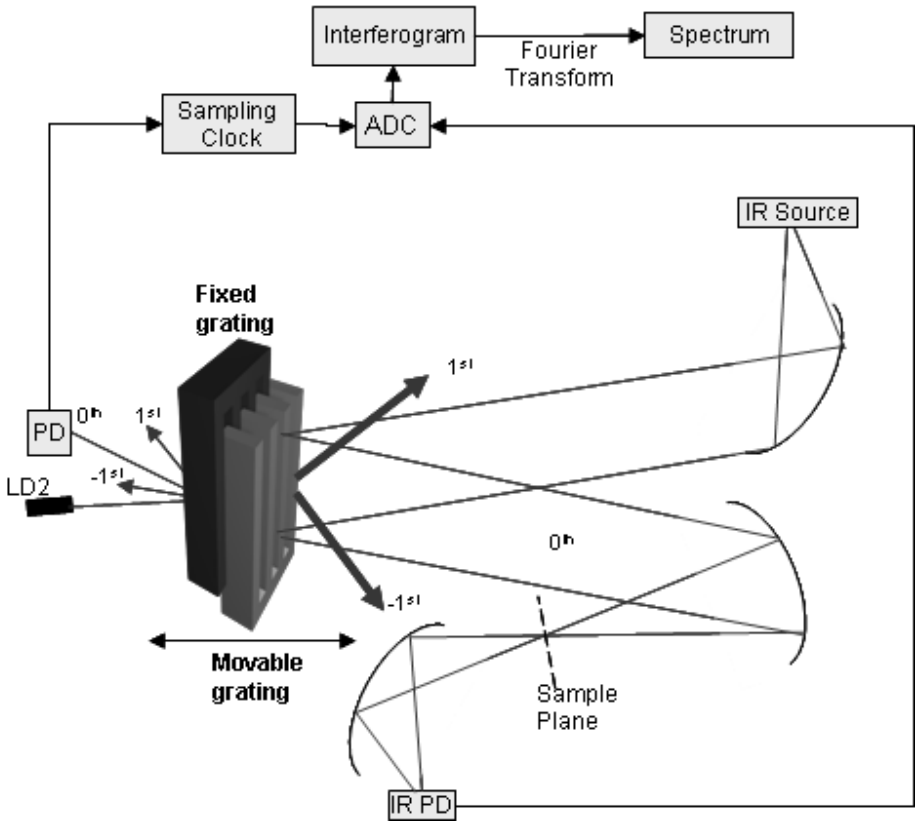

Figure 1.8 - LGI type spectrometer layout

If the interferogram of a perfectly monochromatic source is recorded at infinite extend, it would be a perfect sinusoid whose Fourier Transform yields an infinitely narrow signal, i.e. Dirac delta, at the correct spectral frequency. In reality, there are limitations for the spectral resolution. The limited grating displacement and beam divergence form the basic limitations. Limited displacement of the grating corresponds to an apodization of the sinusoid with a box window. This windowing means a convolution of the Dirac delta with a sinc function in the spectral domain. Since the width of the resulting sinc function is inversely proportional to travel range of the grating, the spectral resolution limit can be stated as in (1.10).

$$\Delta k = \frac{a}{O.P.D.} = \frac{a}{2d_{\max}} \tag{1.10}$$

where Δk stands for the spectral resolution based on first zero crossing width of the FTS of a monochromatic source, OPD is the maximum optical path difference, d_{max} is the maximum travel range of the grating, and "a" is a constant factor that varies with aperture size and shape effects. In this thesis we assume a=1 which means there is no other windowing function that is effecting the resolution. For a sinc function the full width at half maximum (FWHM) can be related to zero crossing width by the following relation.

$$FWHM = 1.67\Delta k \tag{1.11}$$

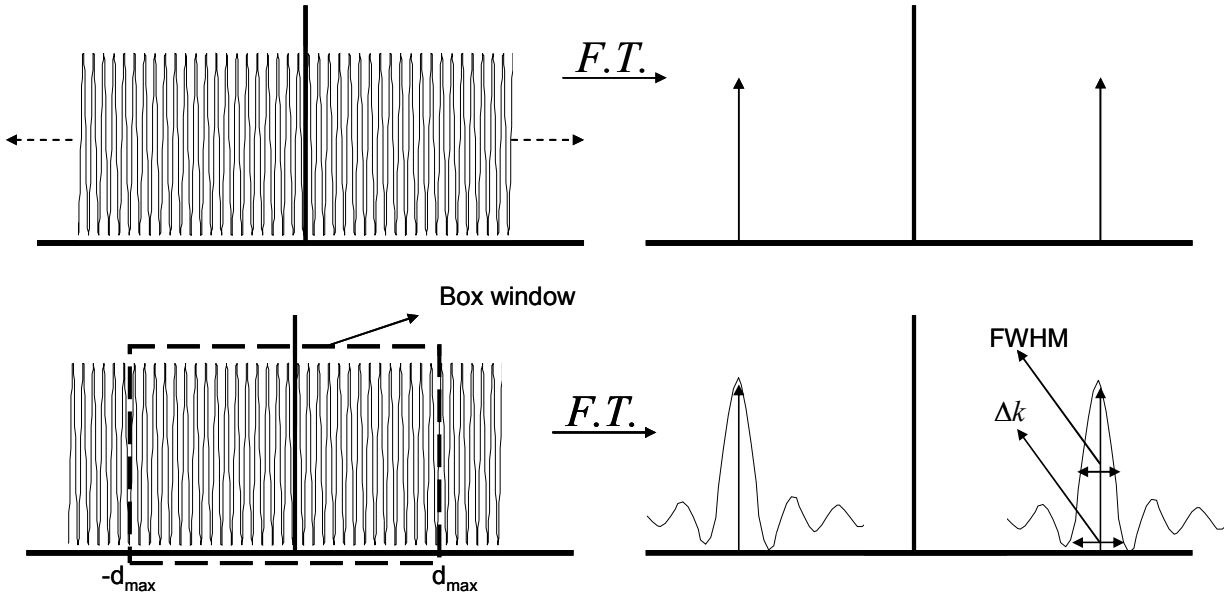

Figure 1.9 – The effect of limited grating displacement on the spectral resolution. Zero crossing resolution and FWHM of the spectrum are shown in lower right figure.

A point source can be used to create a perfectly collimated beam using a positive lens or curved mirror. However, a point source physically is not possible to create and the finite size of the source prevents forming a perfectly collimated beam. A diverging beam exercises infinitely many different optical path lengths and this causes a broadening in the spectral resolution [5]. For a nearly collimated beam illuminating the grating with the divergence angle of $\pm\alpha_{divergence}$, the OPD limited spectral resolution Δk and the minimum wavelength of measurement set a limit on the divergence angle as given by

$$\alpha_{divergence} \leq \sqrt{\frac{\Delta k}{k_{\max}}} \tag{1.12}$$

where

$$k_{\max} = \frac{1}{\lambda_{\min}} \tag{1.13}$$

The Numerical Aperture (NA) of the beam illuminating the LGI can be calculated taking the sine of the divergence angle. NA can be approximated as equal to divergence angle for small angles.

$$NA = \sin(\alpha_{divergence}) \cong \alpha_{divergence} \tag{1.14}$$

Wavelength dependency, asymmetries in the interferogram, sampling errors, stationary and dynamic mechanical impurities, shadowing, polarization effects, and angle of incidence also bring discrepancies and limitations for the computed spectrum. There are several works addressing some of these problems and correction methods [9]-[13]. Polarization effects due to the vector nature of electromagnetic waves can be ignored due to large feature size with respect to the interested wavelength band. Otherwise, this would be an additional issue that broadens the spectral resolution [8]. Wavelength dependent nature of LGI can be corrected by creating look-up tables after a system characterization and feeding the look-up table into the post-processing. Further related work will be presented in Chapter 2.

1.2 LGI in MEMS Literature

MEMS based LGI spectrometer idea is first coined by Manzardo [14]. The details of the work are given in [15]. The device works on electrostatic comb driving principle and performs 72.5 μm in plane stroke. It is reported that a resolution of 1.6 nm at a wavelength of 400 nm and of 5.5 nm at 800 nm is obtained. The operation band is described as between 380 nm and 1100 nm. However, since the thickness of the device is used as the reflective part, the aperture size is limited to 75 μm in one dimension. The device is commercialized

as miniaturized near infrared (NIR) and mid infrared (MIR) spectrometers [16] (Figure 1.10).

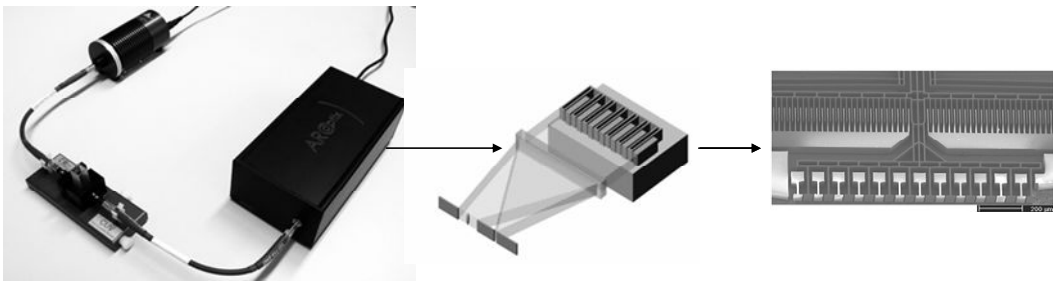

Figure 1.10 – LGI based spectrometer developed by Manzardo's group [16]

Recently a group from National University of Singapore has demonstrated electromagnetically actuated MEMS device which is able to move 100 μm out of plane (Figure 1.1)[17]. It is reported that a tunable laser source whose wavelength changes from 1520 nm to 1590 nm is measured with 0.4% precision using a reference laser source of 533 nm wavelength.

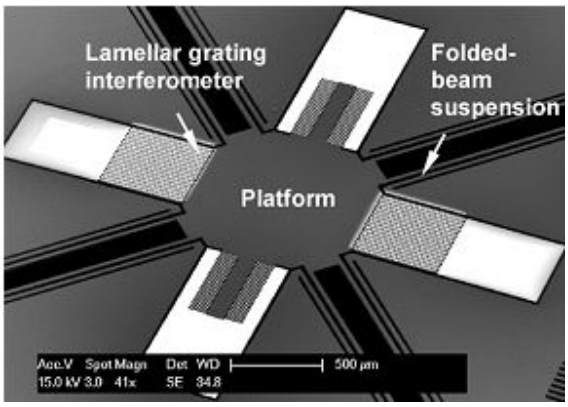

Figure 1.11 – MEMS LGI interferometer developed by F. Lee et. al. [17]

A novel LGI device has been developed in Optical Microsystems Laboratory (OML) of Koç University [18] (Figure 1.12). The device utilizes the grating fingers as the electrostatic driving combs; so that, the device can move 106 μm peak-to-peak out of plane at ambient air pressure and 1.1 kHz with 28 V square wave excitation. The device suffers from dynamic deformation. Thus, only 12.2 nm resolution at 638 nm could be obtained. The concept is licensed by Fraunhofer Institute for Photonic Microsystems (IPMS) [20].

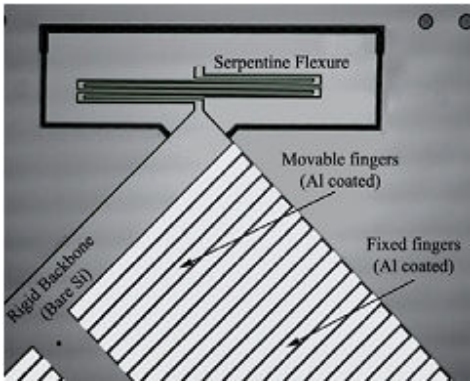

Figure 1.12 - MEMS LGI interferometer developed by Ataman [18]

In this thesis work, the design developed by Ataman is enhanced for a better performance as a part of MEMFIS project. MEMFIS is an FP7 project which is funded by European Commission. The project started at 2008 as a 3 year project and aims to produce ultrasmall FT-IR spectrometers based on MEMS technology [21].

1.3 Novel Design Overview and Contributions of the Thesis

LGI-MOEMS design is composed of stationary and movable parallel fingers. Movable fingers are carried via a backbone and the motion is transferred to the backbone through the flexures which has a pantograph structure. The simplified exemplary drawing of the whole device is shown in Figure 1.13.

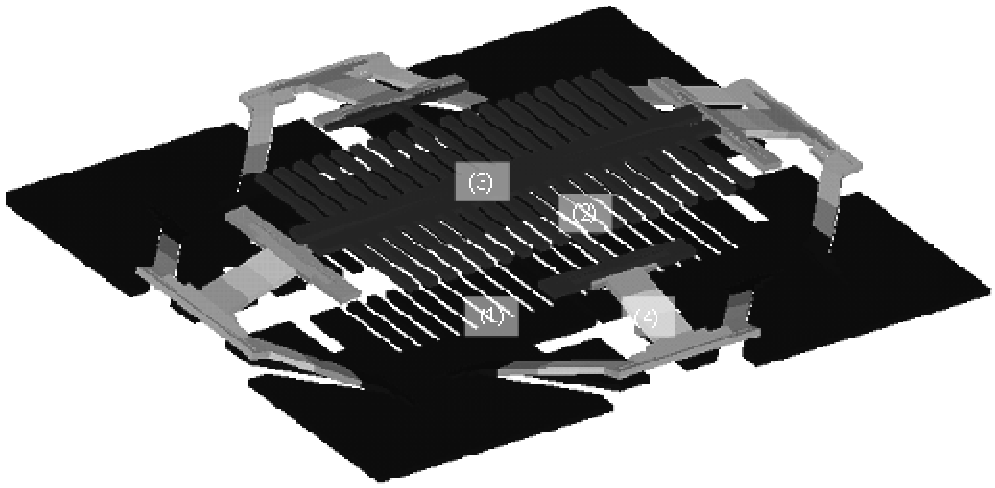

Figure 1.13 - (1) Fixed fingers and Silicon die, (2) Movable fingers, (3) Backbone, (4) Pantograph springs

This novel structure has the following unique features:

1. The mechanical design is optimized by introducing pantograph type spring suspensions so that the structure allows ±500 μm mechanical path difference. This corresponds to 10 cm^{-1} theoretical resolution which should perform 10 times better measurement than the previous FTS device demonstrated in Koç University.
2. Decoupling structures are developed to reduce the dynamic deformation at the grating fingers and peak to peak deformation is minimized down to 300 nm. Thus, a limiting factor for spectral resolution is eliminated.
3. Mechanical stop structures are designed to limit the deflection and increase shock and vibration resistivity of the device.

4. Grating finger shape and grating period size are studied to enhance spectral resolution and light efficiency, and based on the studies theoretical limits are established for LGI based FTS systems.
5. Comb fingers are placed around the pantograph spring suspensions and electrically isolated from the grating fingers. Therefore, both of the finger sets will be utilized for electrostatic actuation and will ease the operation in ambient air pressure.

The details of the design study are explained in the following chapters. Chapter 2 gives the optical design study and grating structure optimization first by explaining the analytical background and then demonstrating the numerical simulation results. Chapter 3 explains the mechanical design from several aspects. Chapter 4 investigates the electro-mechanical properties of the design. The thesis is finalized with the Conclusions chapter that summarizes the thesis and discusses the advantages of the design.

Chapter 2

2 LGI MOEMS DESIGN OPTICAL PROPERTIES

2.1 Analytical background

The performance of the LGI-MOEMS device highly depends on the grating period and wavelength relation. The fundamental compromises are present between the reflected light efficiency, the order separation, and the spectral resolution. Sufficiently small grating period is needed to isolate the 0^{th} diffraction order from the other orders. On the other hand, as the grating period becomes smaller, total gap area between the fingers also increases which results as the loss of light. The spectral resolution also becomes worse with smaller grating periods.

The first diffraction orders appear at the angle α:

$$\alpha = \sin^{-1}(\frac{\lambda}{\Lambda}) \tag{2.1}$$

where λ is the wavelength and Λ is the grating period. On the other hand, the divergence angle of the light source is specified as ±2.5 degree for the MEMFIS project based on (1.12) and assuming 4000 cm^{-1} maximum wavenumber and 8 cm^{-1} resolution requirements. Since the 0^{th} order is needed for FTS, divergence angle should be smaller than the 1^{st} order angle (α) as shown in (2.2). Otherwise, wide 0^{th} order caused by beam divergence would mix with the higher orders and the separation of the orders would not be possible.

$$\begin{aligned} \alpha_{divergence} &\le \alpha \\ \alpha_{divergence} &\le \sin^{-1}(\frac{\lambda}{\Lambda}) \end{aligned} \tag{2.2}$$

This condition forces the grating period to be less than 57 μm for the specified beam divergence angle and minimum wavelength that will be measured.

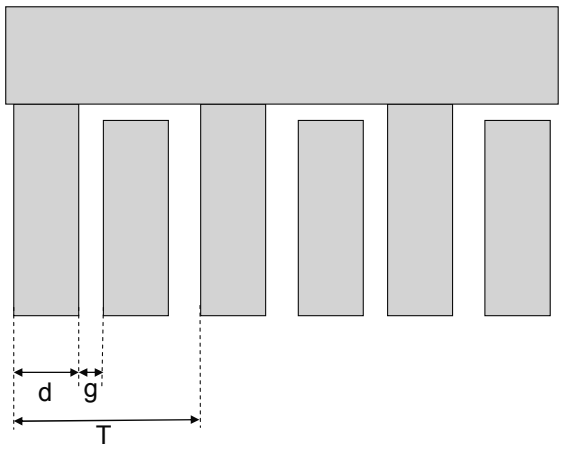

Figure 2.1 - Sketch of the LGI device grating (d: finger width, g: gap width, T: grating period)

The preliminary light efficiency can be deduced from the ratio between the reflective and the full area. Since possible minimum pitch (shown as g in Figure 2.1) is 5μm due to the fabrication limitations, gratings with smaller period have less reflective area compared to gratings with larger period. Including the non-reflective back-bone area (20% of the whole grating area) and the 90% assumed coated grating reflectivity, the correlation is computed as using (2.3) and shown in the Figure 2.2.

$$Efficiency = (\frac{d}{d+g}) \times reflective\ area\ ratio \times reflectivity \quad \textbf{(2.3)}$$

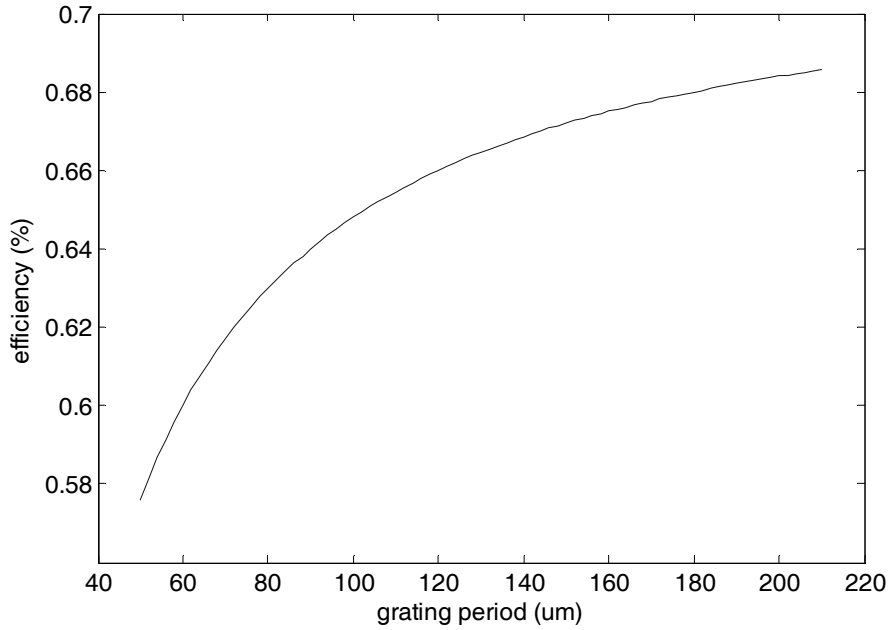

Figure 2.2 – Light efficiency based on the reflections and grating area-to-gap ratio

Even though the light budget is determined primarily according to the reasons explained above, diffraction effects come into the play when the wavelength-to-grating period ratio decreases. The diffracted light that goes through the grating creates the images and the phase reversed images of the grating structure at some specific distances. These images are called as Talbot images (Figure 2.3). The Talbot image distances, z_{talbot}, are found with the following formula:

$$z_{talbot} = n\frac{2\Lambda^2}{\lambda} \tag{2.4}$$

where n is an integer. If the grating period is not selected correctly, the distance between the two finger sets of the LGI device may become closer to the distance of phase reversed

Talbot image. This results in regression of the efficiency and resolution. Therefore, numerical analyses of the system are carried to find the best grating period size.

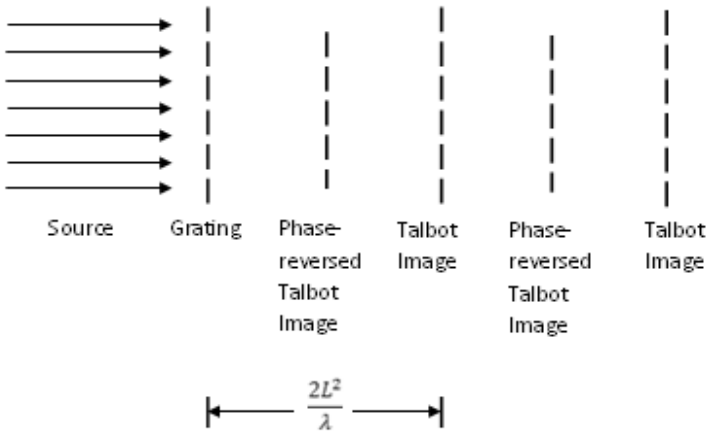

Figure 2.3 - Talbot images of an amplitude grating illuminated by a plane wave. *L* is the grating period in the Talbot distance formula [25].

2.2 Numerical analyses

A scalar wave propagation simulation code is written in MATLAB^{TM} in order to understand the effects of grating structure on spectrum measurements. The code basically models the Fresnel propagation of the wave using the algorithm shown in Figure 2.4.

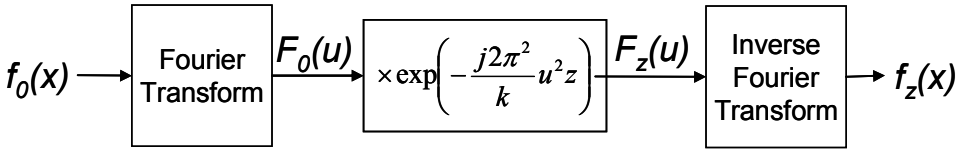

Figure 2.4 – Fresnel propagation algorithm

The effect of the divergence of the source is also taken into account in the simulations. However, polarization effects and finite thickness of the grating fingers are ignored. The

confidence of the MATLAB^{TM} simulations is increased with the verification by COMSOL^{TM} FEM with vector diffraction methodology.

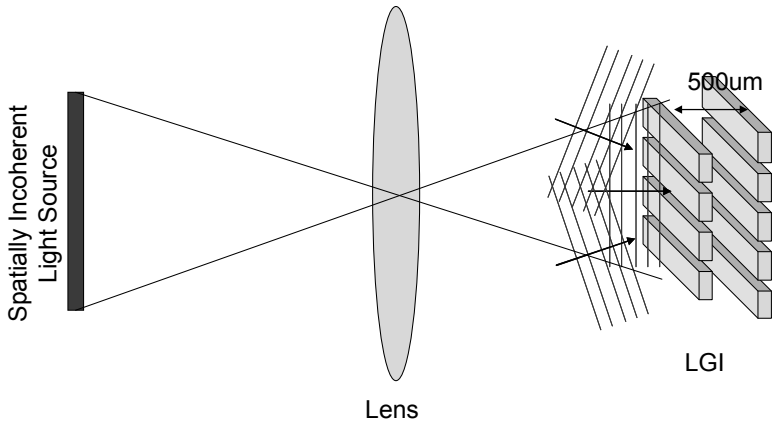

Figure 2.5 – Cartoon drawing of the modeled system

Using the wave propagation simulation code, plane waves at certain different angles are sent onto the grating fingers (Figure 2.5). The mechanical path difference is swept from 0 to 500μm. At specific distances, reflected light instances are used to create the interference pattern at the far field. Example far field patterns for normal incident wave are shown in Figure 2.6.

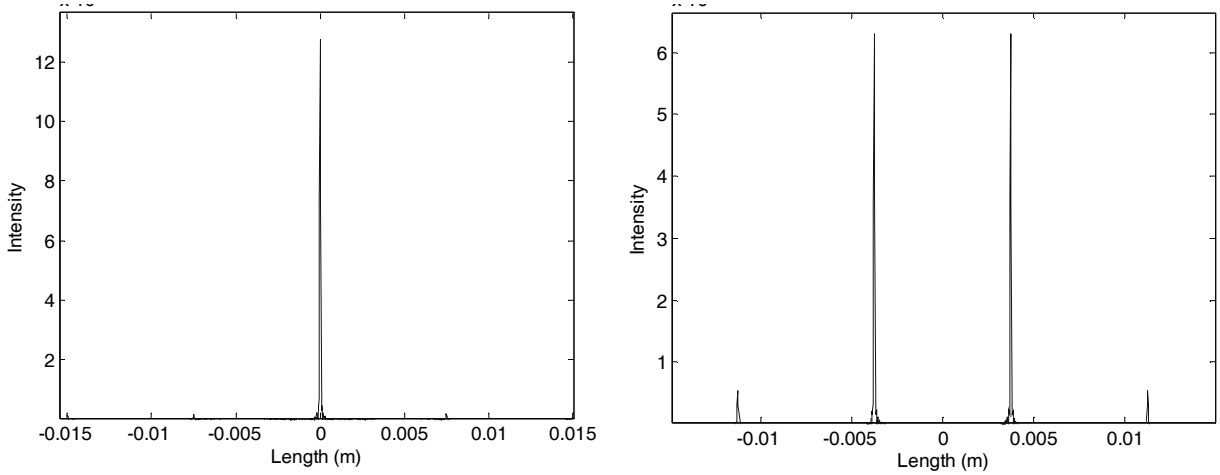

Figure 2.6 - Far field intensity distributions for 100um grating period and 2.5 µm wavelength for constructive (left) and destructive (right) interference cases.

Figure 2.7 shows the far field pattern of 11 different plane waves, incident on the grating at 11 different angles in the range of ±2.5 degrees. Even though there are infinitely many angles, the incident light is approximated with 11 distinct angles for the ease of the computation. Then, the resulting far field pattern is windowed such that the 0^{th} orders are collected and the intensity is calculated by integrating the intensity field inside the window. This intensity value corresponds to one data point on the interferogram. Thus, this operation is repeated while changing the optical path difference and an interferogram is acquired (Figure 2.8).

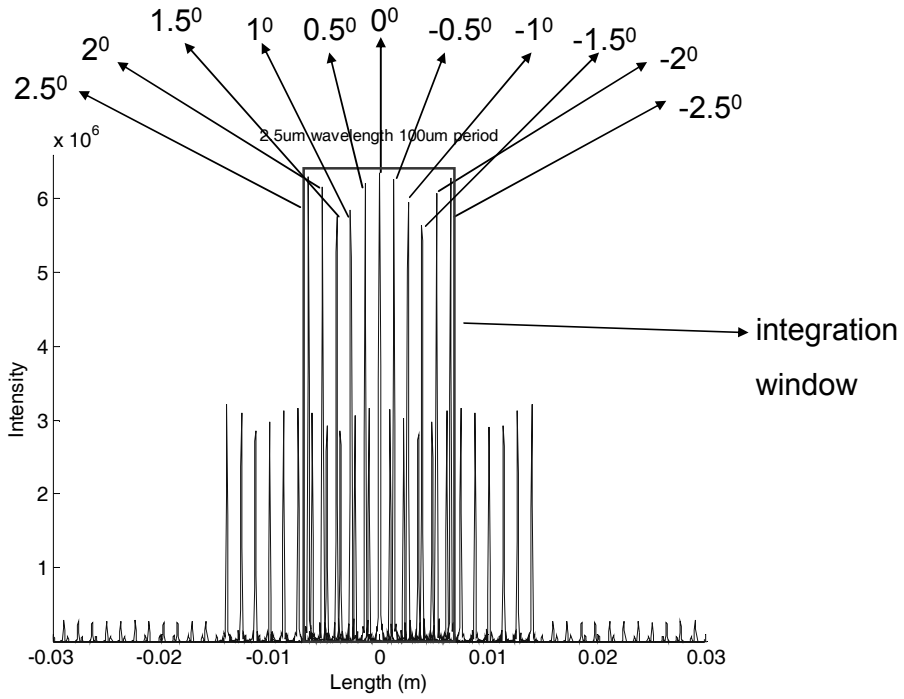

Figure 2.7 – Far field pattern for 100um grating period, 2.5um wavelength, and ±2.5^0 beam divergence for an intermediate level of optical path length difference.

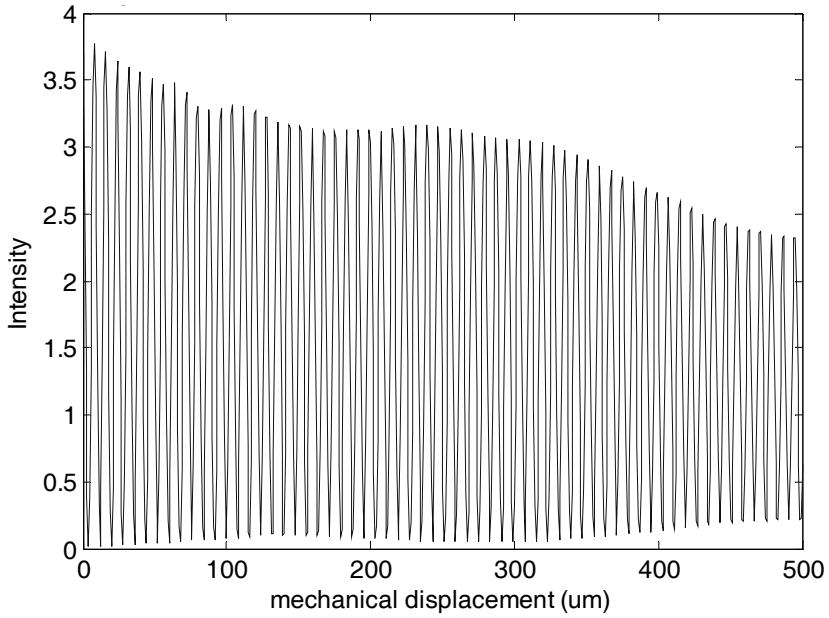

Figure 2.8 – A sample interferogram for 16μm wavelength, 150μm grating period and ±2.5^0 beam divergence.

The Fourier transform of the interferogram gives the spectrum of the light. The spectrum computed using the interferogram above is shown in Figure 2.9. The zero crossing width of the spectrum is defined as the resolution limit and computed by finding the FWHM of the resulting spectrum and using (1.11). In Figure 2.10, barely resolvable two wavelengths separated by the resolution limit, or a zero crossing width amount, are shown.

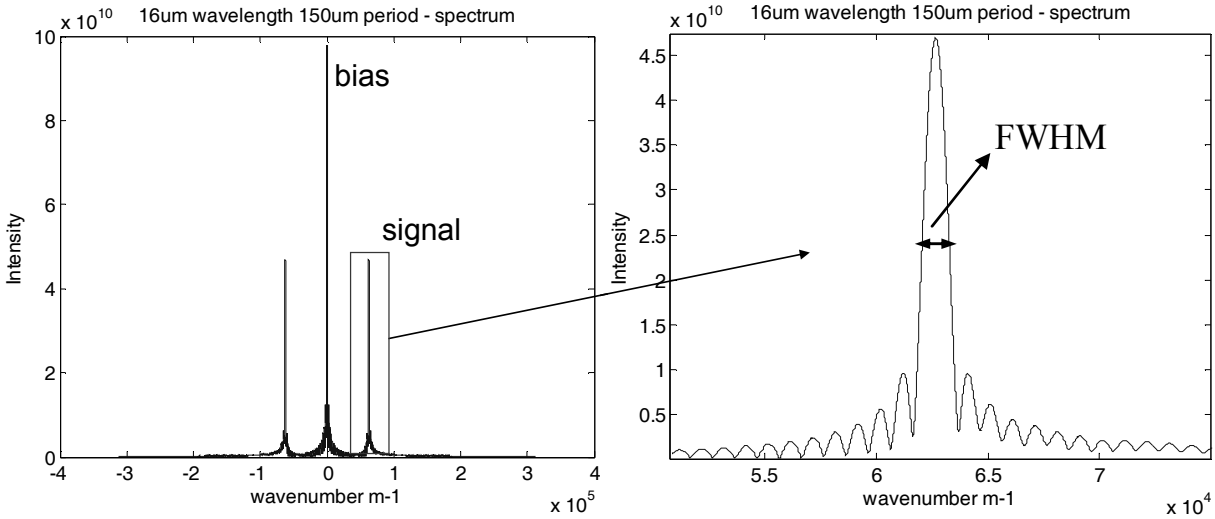

Figure 2.9 – A sample spectrum where the resolution is computed as 12 cm^{-1} for 16 µm wavelength, 150 µm grating period, and ±2.5^0 beam divergence (intensity levels are arbitrary)

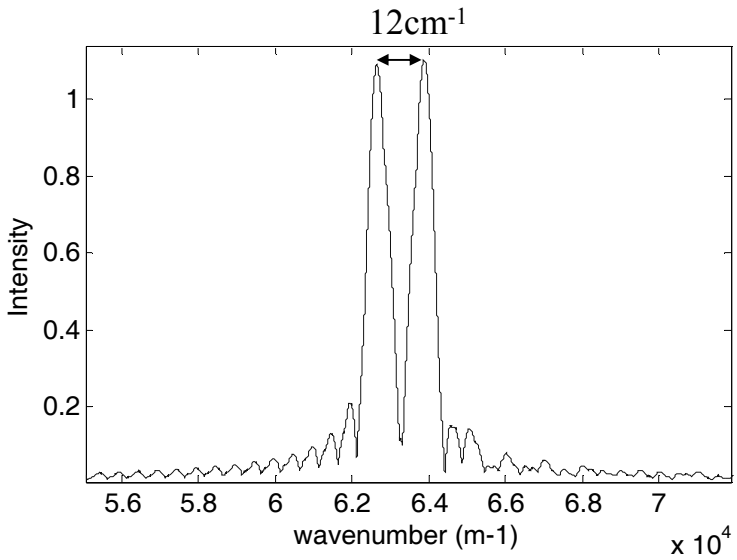

Figure 2.10 – Analysis of a spectrum that contains two different frequencies that is separated by the resolution amount (Δk) with 150 µm grating period and ±2.5^0 beam divergence (intensity levels are arbitrary)

The described simulation steps are repeated for different grating periods and wavelengths of interest (from 2.5 μm to 16 μm). Resolution and signal to bias ratio (SBR) are recorded for each case. Simulations are repeated for 0^0 and $\pm 2.5^0$ divergence angles to see the beam divergence effects. Exemplary interferograms and their Fourier Transforms, or spectra, are given in Figure 2.11. In Figure 2.12, resolution and SBR maps are illustrated for different wavelength and grating period combinations with and without the beam divergence. Note that the small islands in the contour plots are numerical artifacts that occur due to coarse sampling.

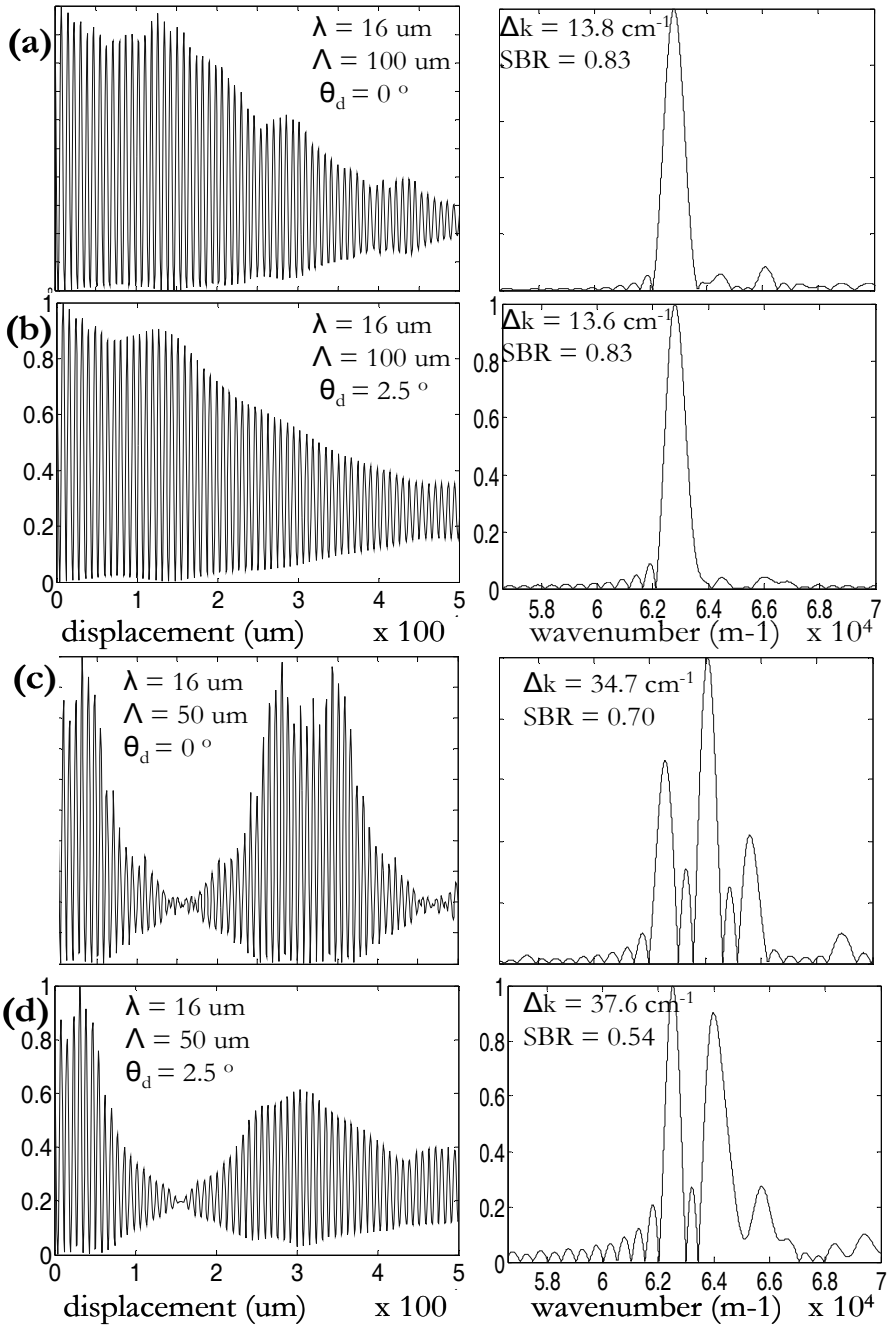
(a)
λ = 16 um
Λ = 100 um
θd = 0 °
Δk = 13.8 cm-1
SBR = 0.83
(b)
λ = 16 um
Λ = 100 um
θd = 2.5 °
Δk = 13.6 cm-1
SBR = 0.83
displacement (um) x 100
wavenumber (m-1) x 10^4
(c)
λ = 16 um
Λ = 50 um
θd = 0 °
Δk = 34.7 cm-1
SBR = 0.70
(d)
λ = 16 um
Λ = 50 um
θd = 2.5 °
Δk = 37.6 cm-1
SBR = 0.54
displacement (um) x 100
wavenumber (m-1) x 10^4

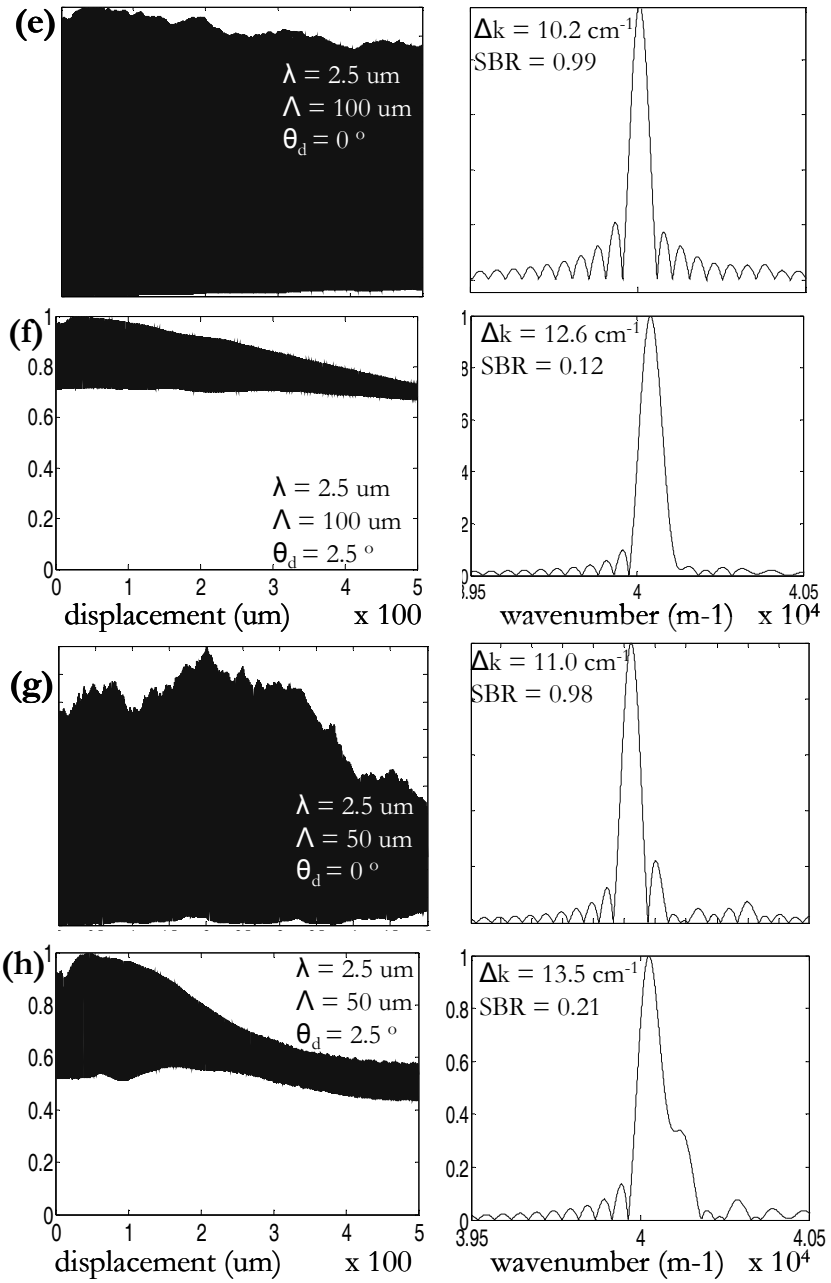

Figure 2.11 – Interferogram and F.T. pairs for various wavelengths (λ), grating periods (Λ) and divergence angles (θ).

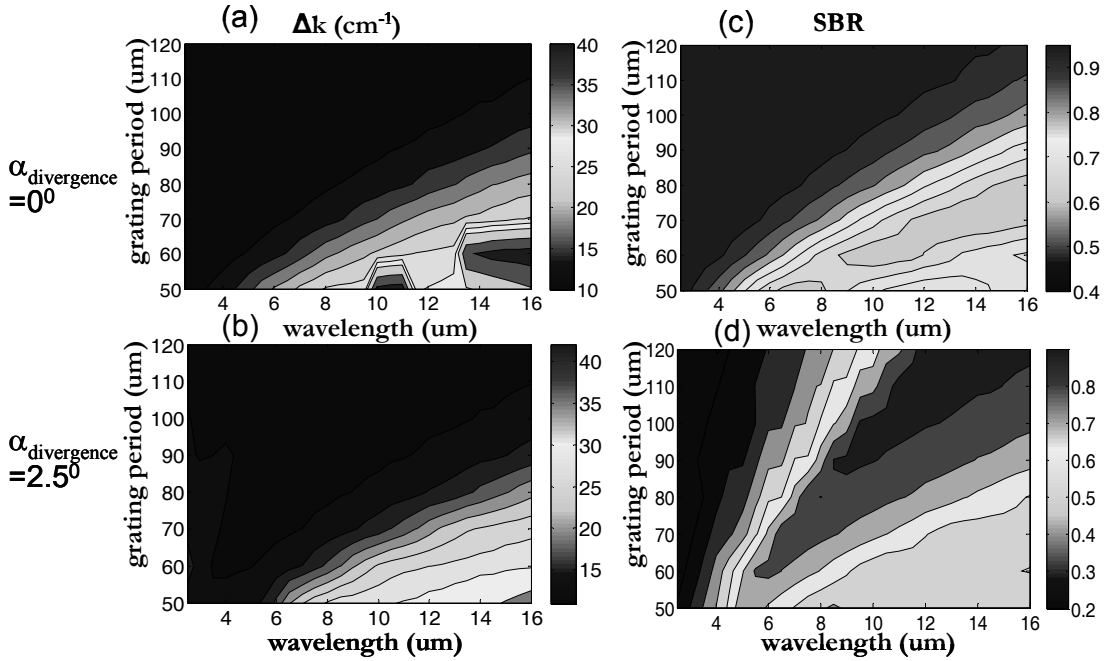

Figure 2.12 – Contour plots as a function of wavelength, grating period and beam divergence angle ($\alpha_{divergence}$) (Left) spectral resolution based on zero crossing width (Δk) in units of cm^{-1}, (Right) Signal to Bias ratio (SBR) of acquired spectrums. Upper plots show the results for zero beam divergence whereas lower plots for $\pm 2.5^0$ beam divergence.

The simulations show that diffraction effects become significant in spectral resolution when the wavelength-to-grating period ratio increases. If the mechanical path length between two grating parts of LGI device reaches half of the Talbot distance, then light is concentrated on the holes of the second grating and escapes out of the device. Therefore interference can not be observed because the light can not return from the second grating. This effect can be seen in Figure 2.11 for wavelength is equal to 16 μm and grating period is equal to 50 μm. In order to prove the validity of the scalar diffraction computations COMSOL^{TM} FEM program is used which also accounts for the vectoral effects and the side walls of the grating structures. Talbot images can be apparently seen in Figure 2.13. From

the simulations it is concluded that the grating period should be picked so that the displacement can not reach phase reversed Talbot image distance.

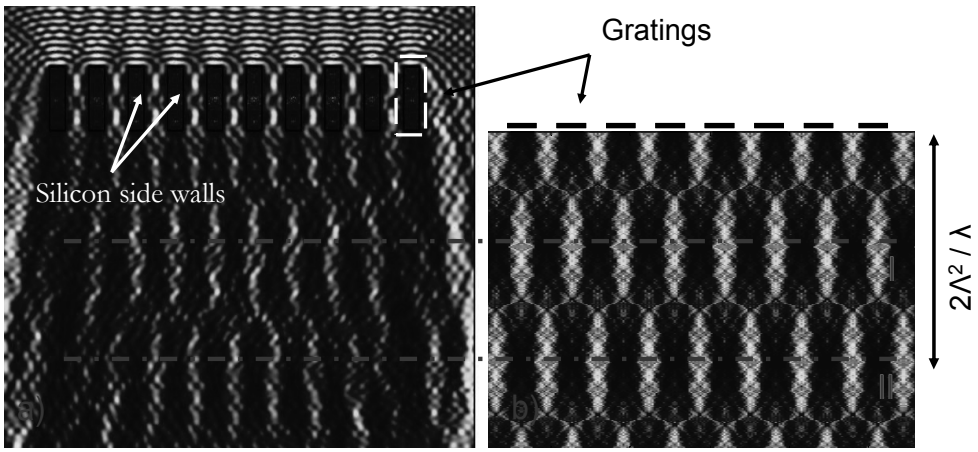

Figure 2.13 – Diffraction patterns of collimated light after passing through square amplitude grating (a) Vectoral Diffraction with COMSOL™ FEM program (b) Scalar Diffraction with MATLAB™ code

Another result that is deduced from the simulations is that the order mixing due to beam divergence is not crucial for the spectral resolution. Although the obligation given in (2.2) is highly violated at the left sides of Figure 2.12 (b), the resolution does not change significantly when compared Figure 2.12 (a). However, at the same regions of Figure 2.12 (d), one can observe lower SBR levels compared to Figure 2.12 (c). Low SBR means poor fringe contrast which uses upper part of the available detector dynamic range and should be taken into account for the system efficiency and measurement accuracy. Also note that the difference in spectral resolutions between first two spectrums of Figure 2.11 is due to numerical artifacts.

As the final decision, 3 design variants will be fabricated: 60 μm, 80 μm, and 100 μm constant periods. After the experimental characterization the variant with the best performance will be chosen. The layouts for 60 μm, 80 μm, and 100 μm devices are shown in Figure 2.14 through Figure 2.16 respectively.

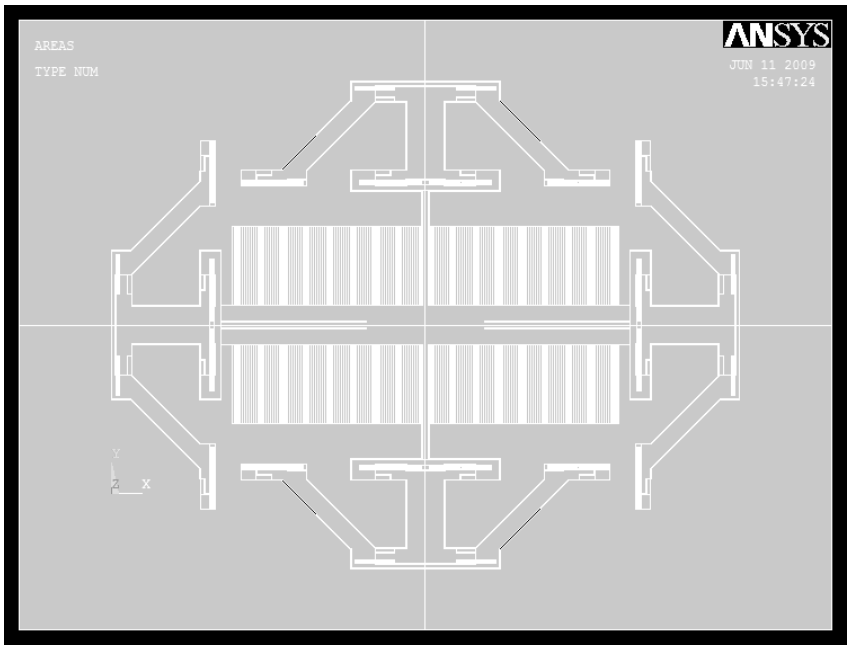

Figure 2.14 – LGI device with 60µm grating period

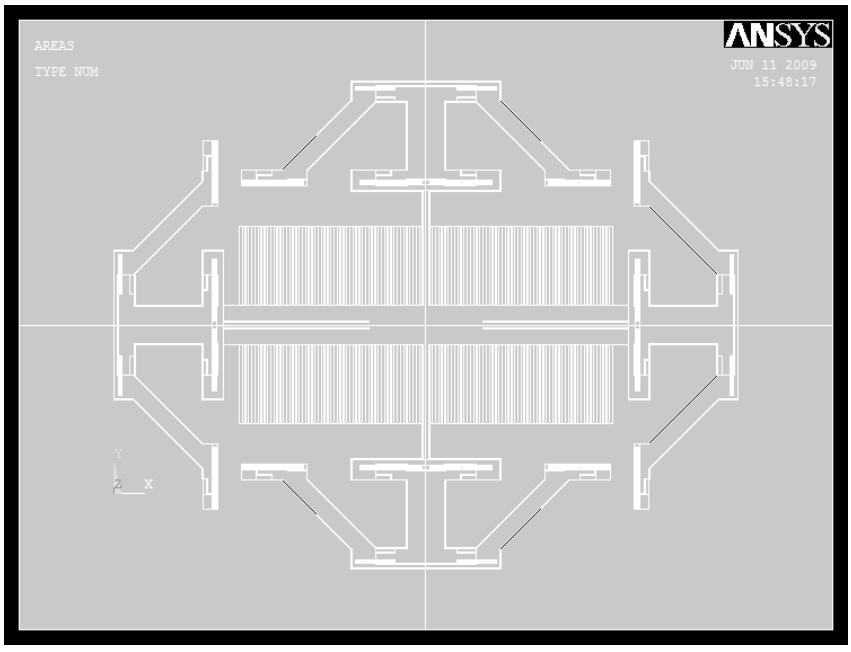

Figure 2.15 – LGI device with 80µm grating period

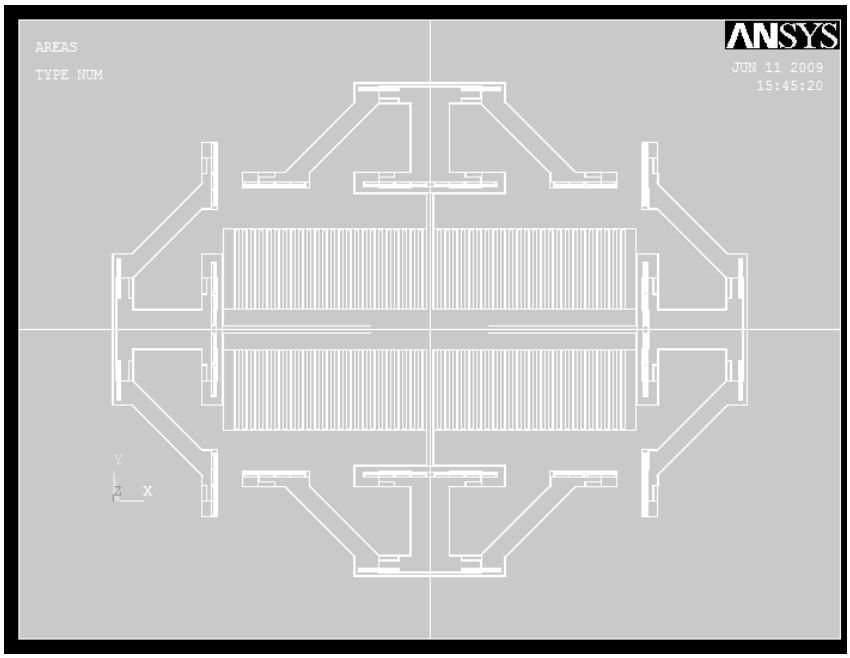

Figure 2.16 – LGI device with 100µm grating period

Chapter 3

3 LGI MOEMS DESIGN MECHANICAL PROPERTIES

The design requirements determined for the MEMFIS project oblige a mechanical structure that can translate ±500 μm with maximum 250 nm non-uniformity over the optically active area that should be kept as large as possible to increase the light efficiency of the device.

Mechanical design is developed using ANSYS^{TM} FEM software. Silicon properties are modelled according to data supplied by Fraunhofer IPMS which are experimentally confirmed.

The LGI MEMS device has two main parts: (1) Grating body, and (2) Pantographs. The pantograph structure, introduced by Fraunhofer IPMS [22]-[24], converts torsional bending at the springs into translational motion and allows high amount of deflection (Figure 3.1). The body is connected to the pantograph structure through the suspensions that absorb the dynamic deformation at the grating fingers. Grating size is determined as 2.5 mm width by 5 mm length, where the backbone is 0.5 mm wide. Therefore, active grating area is 2 mm by 5 mm. Total die size area including electrical connection pads is determined as 11 mm by 11 mm.

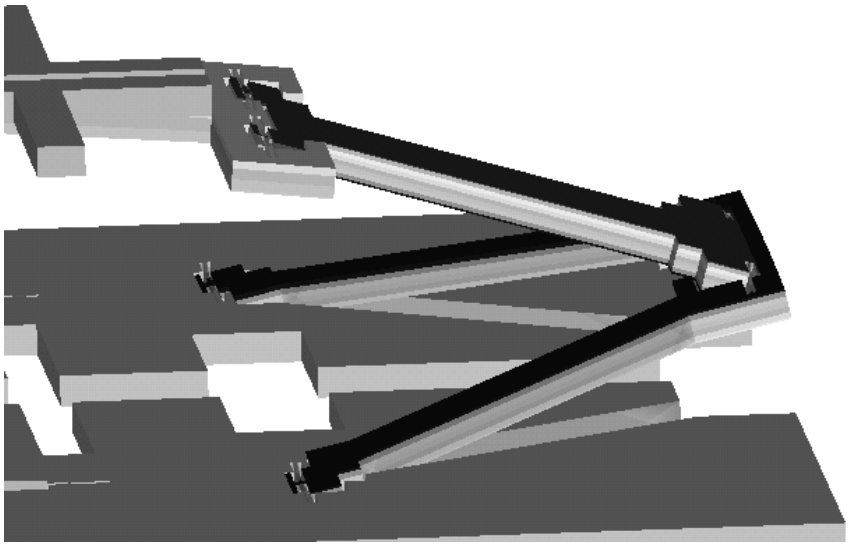

Figure 3.1 – The pantograph structure

3.1 Spring design

The most crucial part of the mechanical design study is the spring design for pantographs. Spring dimensions are determining factor of resonance mode frequencies (e.g. operation frequency, mode separation) and deflection amount. High deflection amplitude can be achieved using soft springs that are not broken due to deformation on the springs. On the other hand, the system should be stiff enough to keep the operation frequency at the requested range. Moreover, softer systems are less shock resistant.

The preliminary design is shown in Figure 3.2. In this configuration, the springs have to be too long to meet the deflection and frequency specifications at a reasonable stress level. On the other hand, elongated springs reduce the separation between the natural resonance modes of the device, such as out of plane and in plane vibrational modes. In order to overcome this handicap, parallel springs are added to the design as shown in Figure 3.3.

Since spring constants are additive in parallel connection, the overall stiffness of the system increased using soft springs which can handle more torsional bending. This methodology helped keeping with the necessary operating frequency and stress limits; and increased the shock resistivity.

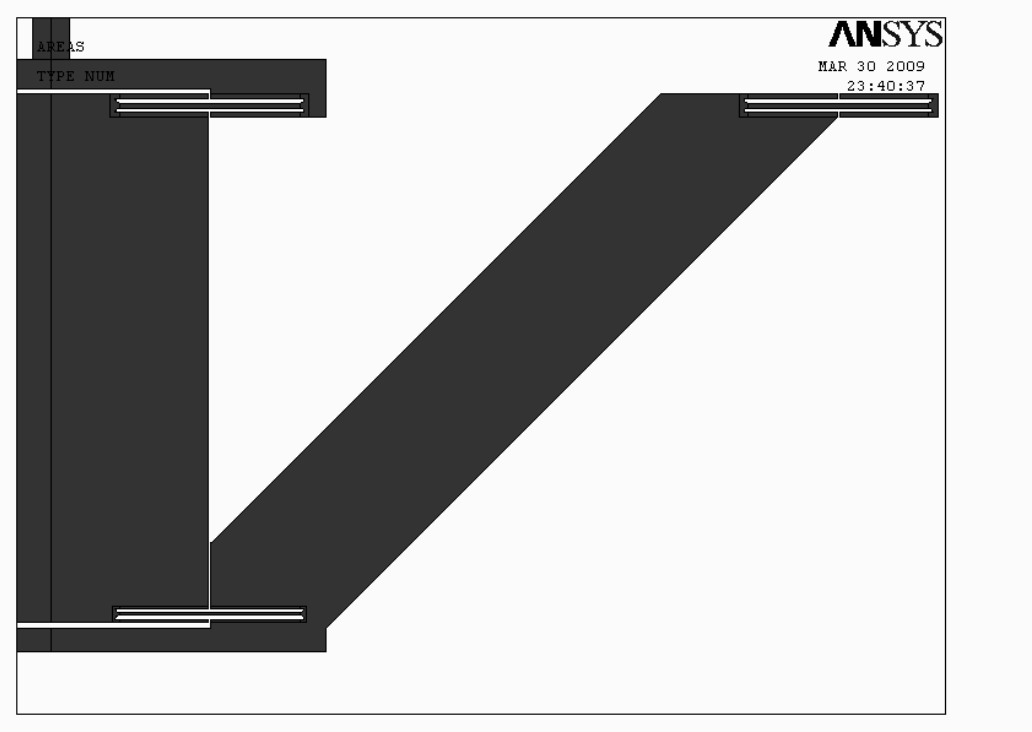

Figure 3.2 – Half of a pantograph deflection arm design using 3 springs

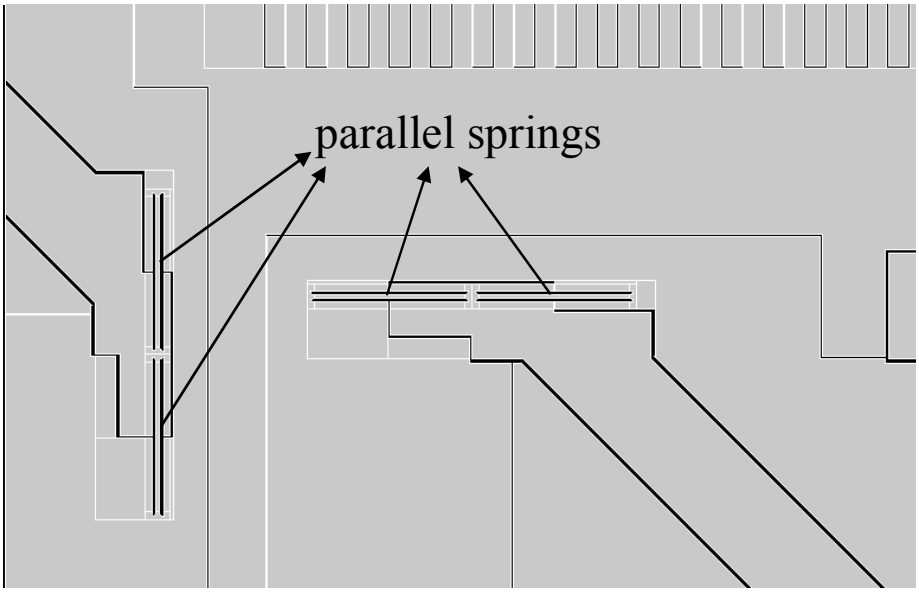

Figure 3.3 – Conventional springs are replaced with parallel springs at connection points to the ground and moving body

3.2 Modal analyses

The device is designed so that the first mode is out-of-plane around 500 Hz. The neighbor mode separation is maintained using appropriate torsional springs that allow 500 μm stroke. The first ten resonant modes are listed below (Table 3.1).

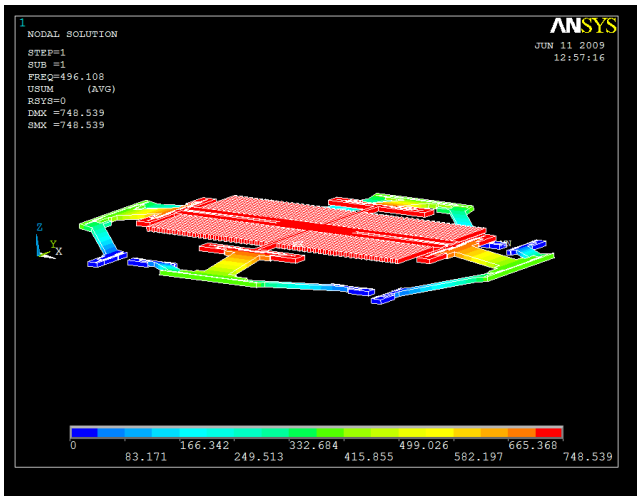

496 Hz Out of Plane

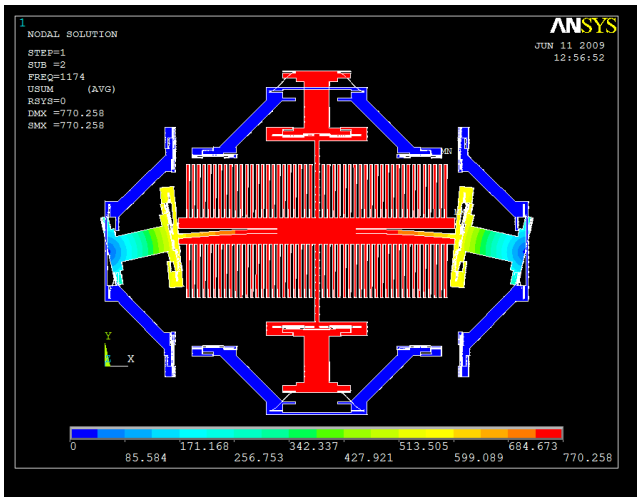

1174 Hz In Plane

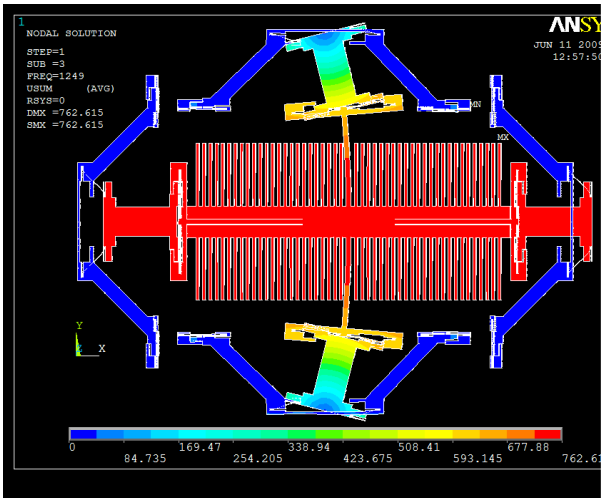

1249 Hz In Plane

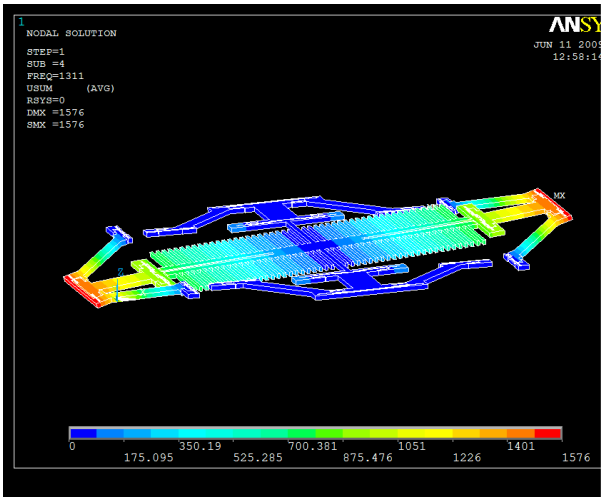

1311 Hz Out of Plane Rocking

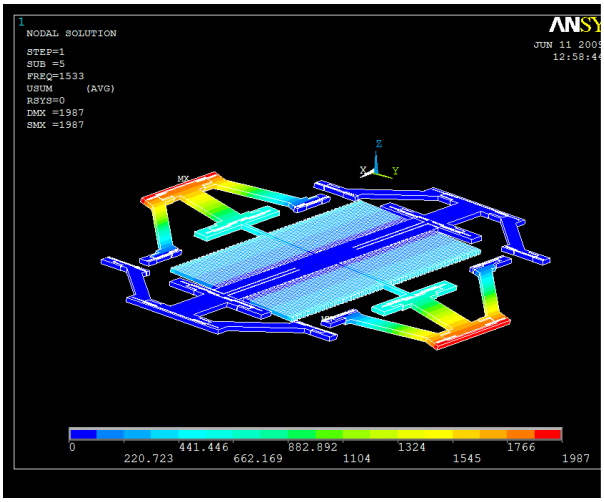

1533 Hz

Out of Plane Rocking

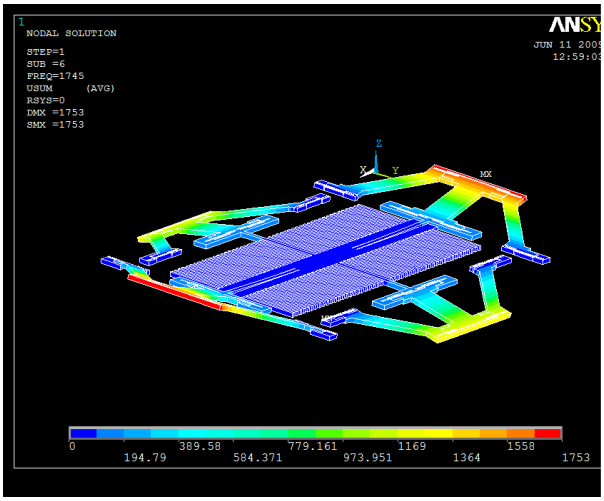

1745 Hz

Out of Plane Pantograph

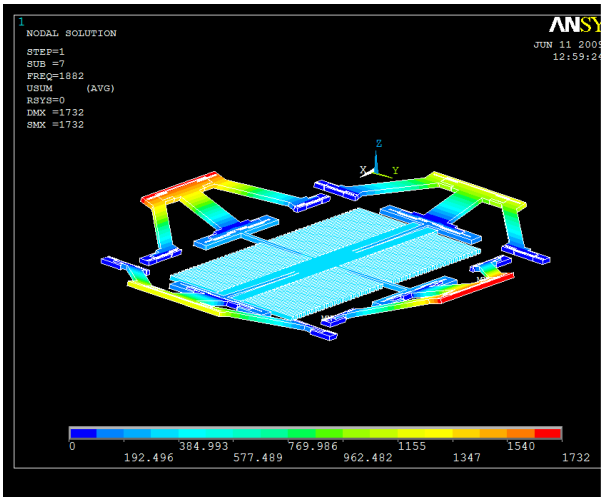

1882 Hz Out of Plane

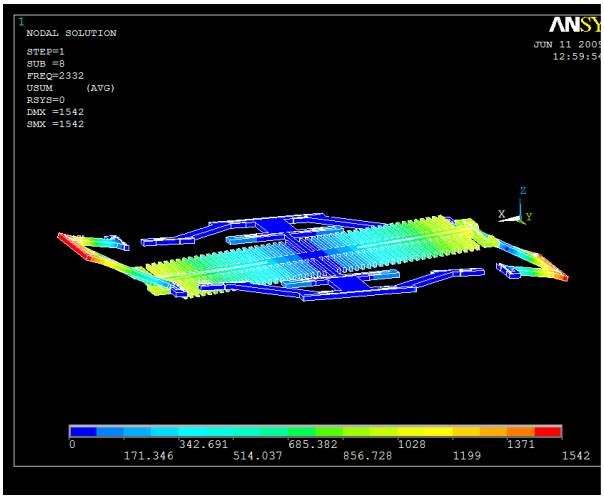

2332 Hz Out of Plane Rocking

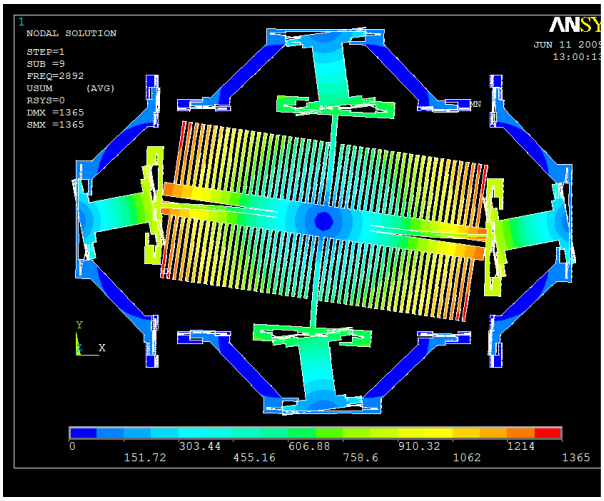	2892 Hz	In Plane Rocking
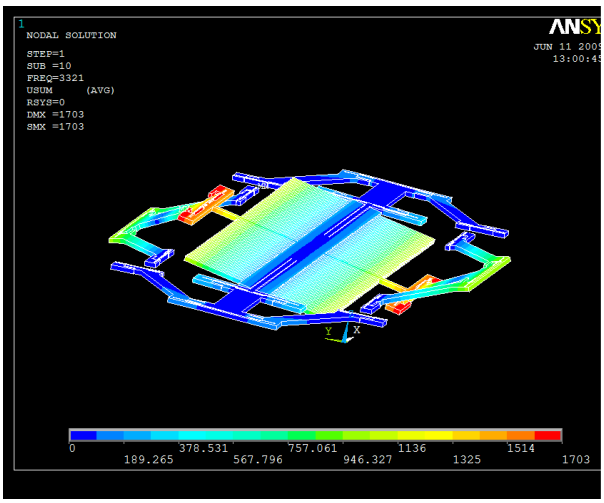	3321 Hz	Out of Plane Rocking

Table 3.1– Resonant modes of the LGI device

3.3 Mechanical stress load

The pantograph springs should satisfy that the maximum stress at the required deflection is under the silicon fracture limit. While maintaining the stress level below the limit, the operation frequency and mode separation are also taken into account. As explained in the section 3.1, parallel spring structure is developed also for this purpose.

In Figure 3.4, the stress levels throughout a pantograph spring are illustrated for 533 µm deflection as shown in Figure 3.5. The maximum stress is found as 1.44 GPa. This stress value stays within the safety limit which is taken as 1.5 GPa.

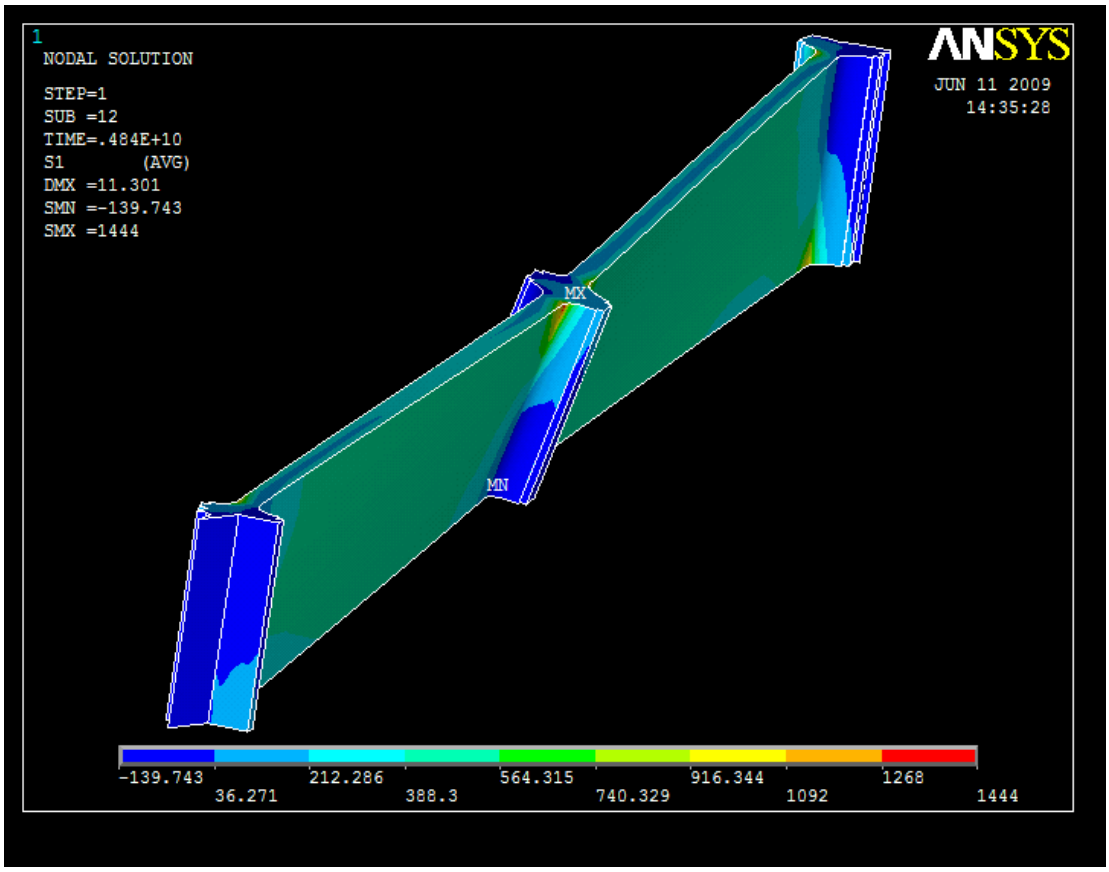

Figure 3.4 - The stress variation among the pantograph spring for 533 µm deflection. (The unit of the colorbar is MPa)

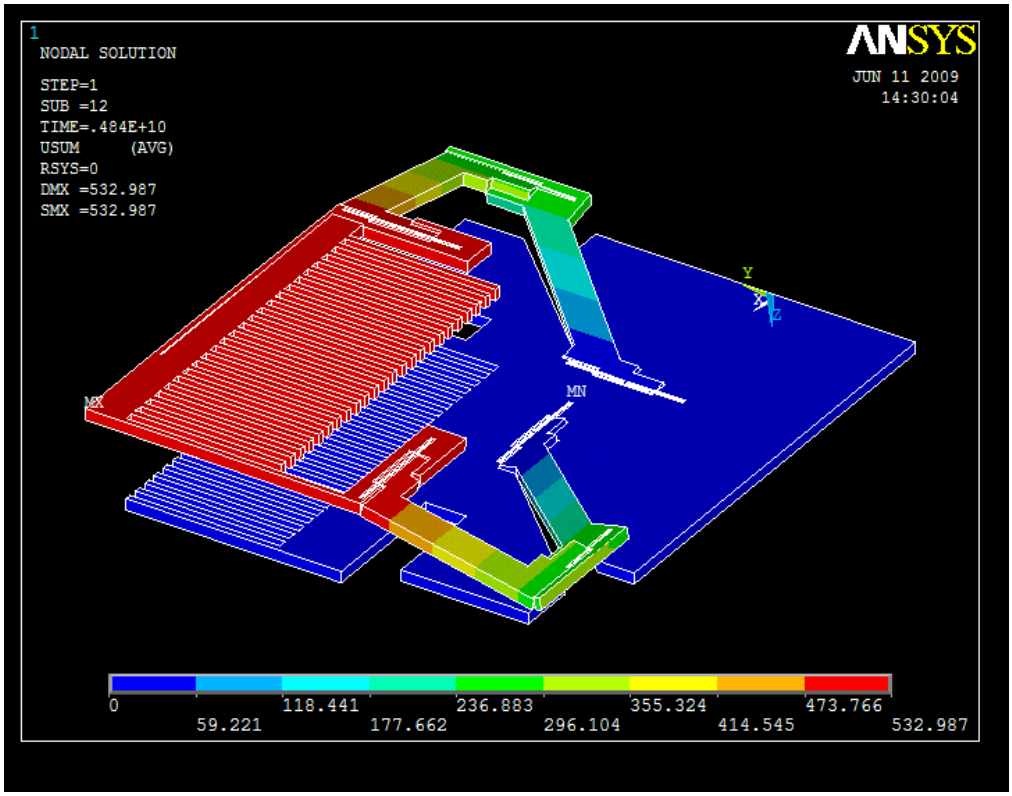

Figure 3.5 - 1/4th model showing 533 µm deflection above the substrate (The unit of the colorbar is µm)

3.4 Mechanical shock resistivity

For the shock-vibration resistivity, mechanical stops are placed around torsional springs (Figure 3.6). After passing a deflection limit, contacts occur at mechanical stop positions as a result of pantograph arms' rotation and translation. The contacts increase system stiffness and preserve the system from shocks and fractures. The contact instances as a result of high deflection can be seen in Figure 3.7, Figure 3.8, and Figure 3.9.

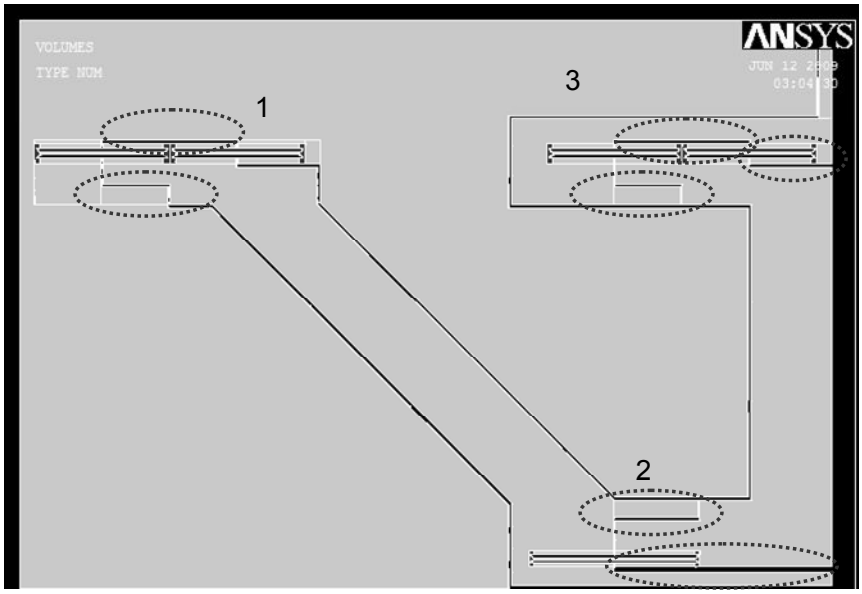

Figure 3.6 – Marked places indicate three regions of mechanical stops

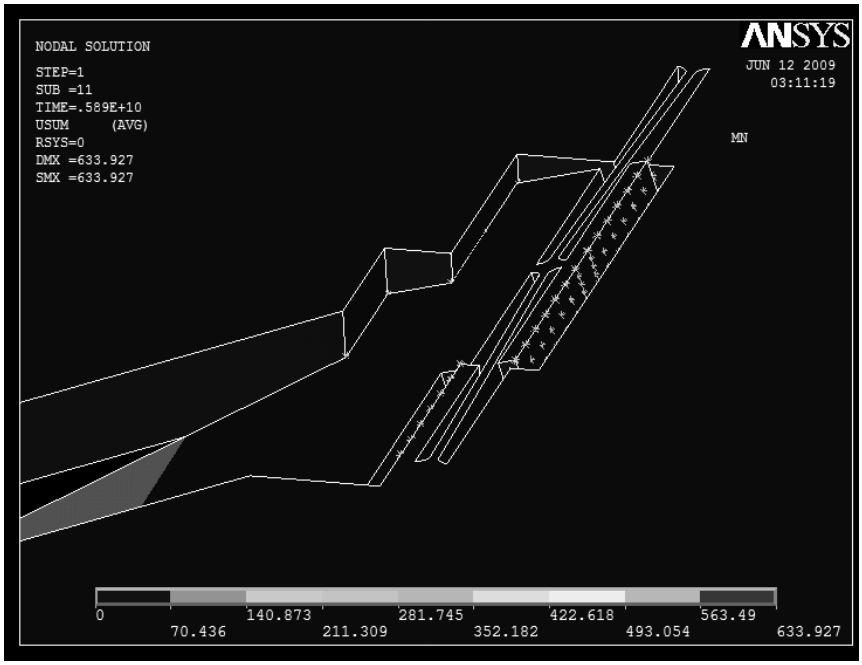

Figure 3.7 - Contact at region 1 (The unit of the colorbar is μm)

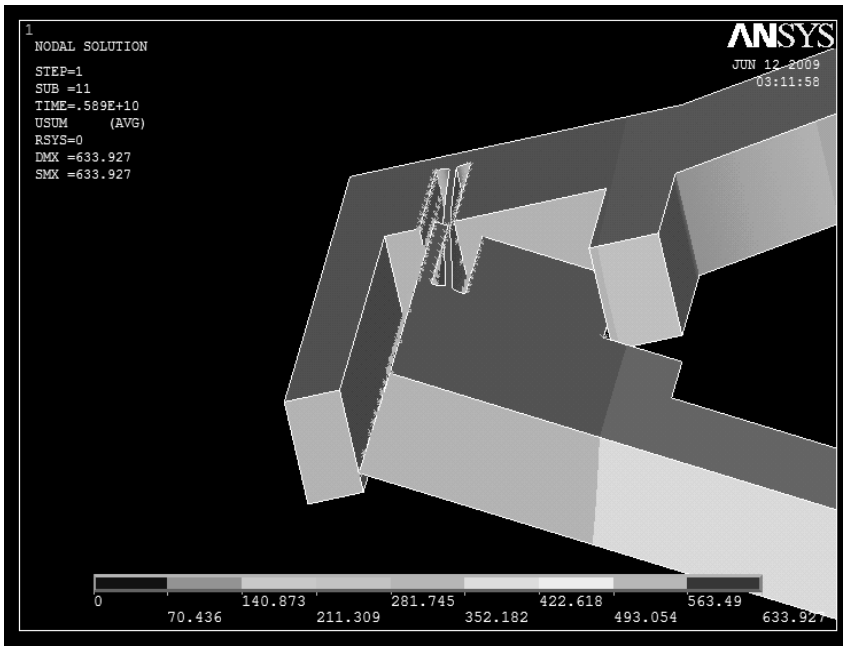

Figure 3.8 – Contact at region 2 (The unit of the colorbar is µm)

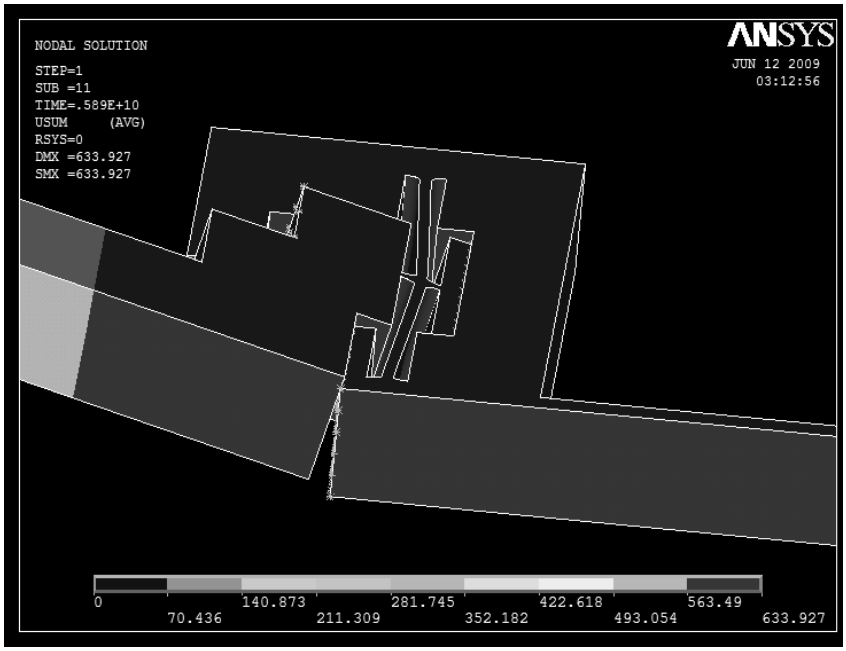

Figure 3.9 - Contact at region 3 (The unit of the colorbar is µm)

The device reaches close to the fracture limits when 500 times the gravitational acceleration is exerted. Mechanical stops significantly prevent unwanted high deflections; however, since the overall stress is already near to the limits, the shock resistance can not be improved much further. The device experiences 1.6 GPa maximum stress at the springs when 1000 times the gravitational acceleration is exerted on the device.

3.5 Dynamic deformation

Another mechanical challenge arises due to dynamic deformation of the device during the operation. The problem is solved by introducing deformation absorbing suspension structures and limiting the finger lengths to 1 mm.

Dynamic deformation is reduced to as low as 300 nm peak to peak along the grating fingers as shown in Figure 3.10.

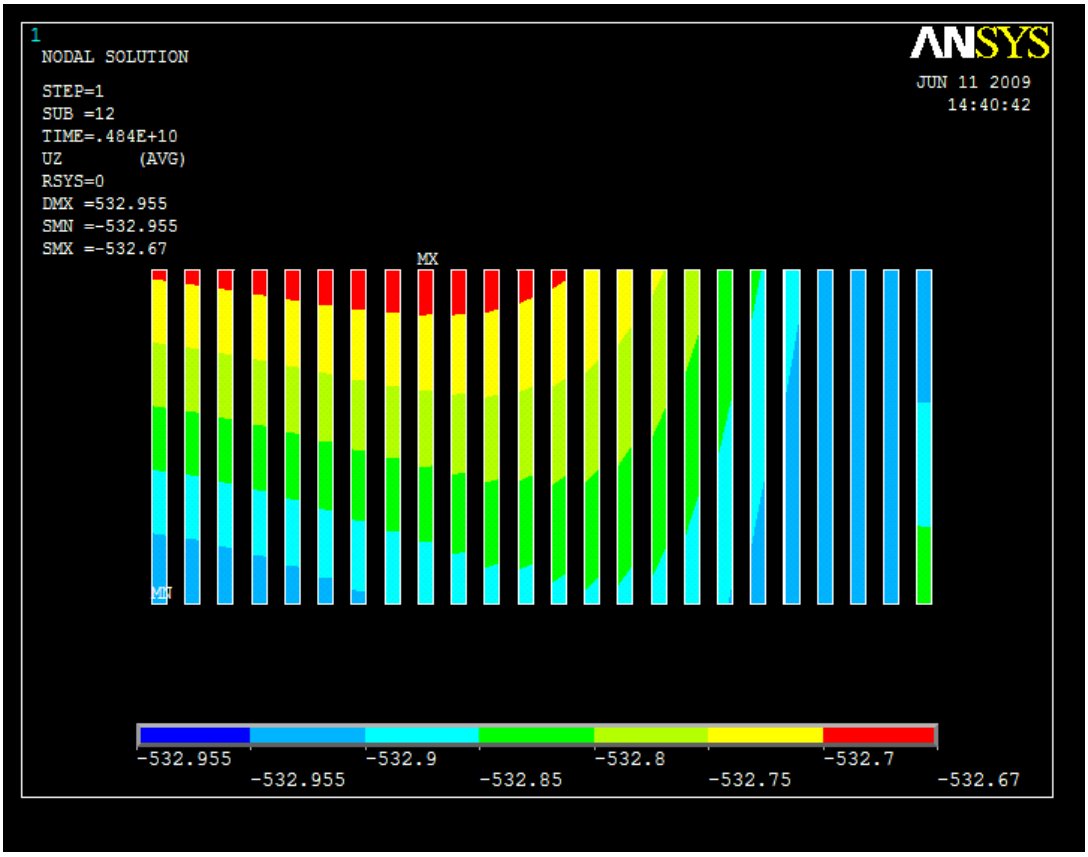

Figure 3.10 - - Dynamic deformation at 1/4th model of the moving fingers (The unit of the colorbar is µm)

Chapter 4

4 LGI MOEMS DESIGN ELECTRO-MECHANICAL PROPERTIES

4.1 Electrostatic comb design

LGI device will be excited by electrostatic comb driving principle. There are two sources for comb drive: (1) The comb drive fingers placed on the pantograph arms and (2) the grating fingers can be used for electrostatic driving. The operation principle is explained in detail in [19]. The layout and electrically isolated parts are shown in Figure 4.1.

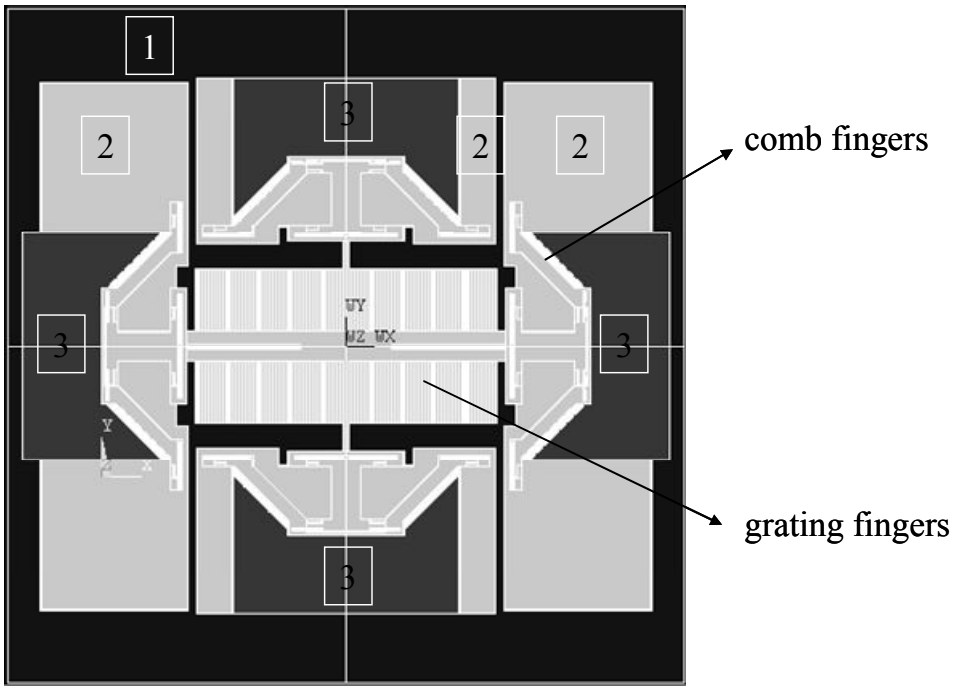

Figure 4.1 – General device layout: (1) Stationary grating fingers (voltage level 1), (2) Moving structure (ground level), (3) Stationary comb fingers (voltage level 3)

4.2 Resonance voltage requirement

Assuming a sinusoidal displacement (z: displacement, v: velocity, a: acceleration, A: translation amplitude):

$$\begin{aligned} z(t) &= A\sin(\omega t) \\ v(t) &= A\omega\cos(\omega t) \\ a(t) &= -A\omega^2\sin(\omega t) \end{aligned} \qquad \textbf{(4.1)}$$

Damping factor can be calculated using (4.2) by assuming a quality factor for the device based on experience with previously studied similar devices: (I_m: mass, b: damping constant, ω: resonance frequency, Q: mechanical quality factor):

$$b = \frac{I_m \omega}{Q} \tag{4.2}$$

Dissipated energy during one period should be equal to the dissipation power integrated over one period time (b is assumed to be constant).

$$E_d = \int_T \mathrm{bv(t)} \frac{\mathrm{d(z(t))}}{\mathrm{dt}} \mathrm{dt} = b \int_T \mathrm{v}^2(\mathrm{t})\mathrm{dt} \tag{4.3}$$

Putting (4.1) and (4.2) into (4.3), dissipated energy can be expressed as:

$$\begin{aligned} E_d &= bA^2\omega^2 \int_T \cos^2(\omega \mathrm{t})\mathrm{dt} \\ &= bA^2\omega \left. \frac{2\omega t + \sin(2\omega t)}{4} \right|_T \\ &= bA^2\omega \left[2\omega t + \sin(2\omega t) \right]_0^{T/4} \\ &= bA^2\omega\pi \\ &= \frac{I_m A^2 \omega^2 \pi}{Q} \end{aligned} \tag{4.4}$$

In one period capacitive energy is injected twice into the system as in (4.5) (C: capacitance, V: voltage across capacitance).

$$\mathrm{E}_i = CV^2 \tag{4.5}$$

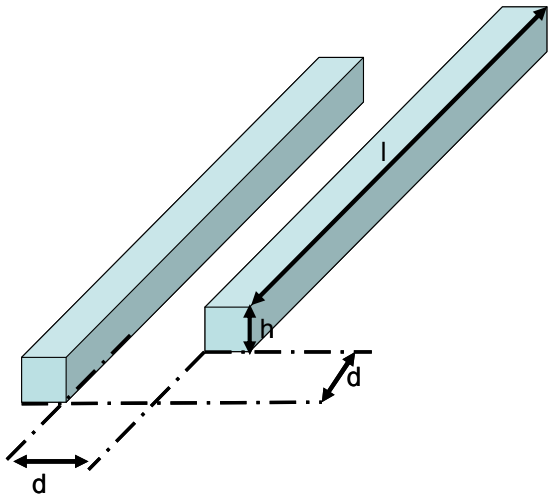

Figure 4.2 – Finger formation

For N moving fingers there are $2N$ capacitors which make the total capacitance:

$$C = 2N\varepsilon\frac{(l-d)h}{d} \tag{4.6}$$

where ((*l*-*d*) is used because for overlapping part length of moving and non-moving fingers, and ε denotes the permittivity of the medium that is air.

Dissipated and injected energies can be equated to find required voltage level to keep the device in resonance motion:

$$\begin{aligned} \mathrm{E_d} &= \mathrm{E_i} \\ bA^2\omega\pi &= CV^2 \end{aligned} \tag{4.7}$$

Finally, the required voltage can be found as in (4.8).

$$\begin{aligned} V &= \sqrt{\frac{bA^2\omega\pi}{C}} \\ &= \sqrt{\frac{I_m A^2\omega^2 d\pi}{2N\varepsilon(l-d)hQ}} \end{aligned} \tag{4.8}$$

An estimate calculation is made using the numbers below:

$I_m = 4.4 \times 10^{-7}$ kg
$A = 500\ 10^{-6}$ m
$\omega = 2\pi f = 2\pi 500 = 3.14 \times 10^{3}$ rad/s
$d = 5 \times 10^{-6}$ m
Q = variable (from 10 to 100)
$\varepsilon = 8.8\ 10^{-12}$ F/m
N = 164 (60um period), 120 (80um period), 96 (100um period)
$l = 10^{-3}$ m
$h = 75 \times 10^{-6}$ m

Grating period	Capacitance
60μm	43pF
80μm	31pF
100μm	25pF

Table 4.1 - Calculated capacitances of the grating fingers

If 220 um long, 5 um wide comb fingers can be placed around the pantographs as shown in Figure 4.1, around 20pF capacitance can be obtained. Using the calculated capacitance values, required voltages at resonance operation can be graphed as shown in Figure 4.3 and Figure 4.4 for low and high quality factors. As the figures imply, the use of grating fingers relaxes the voltage requirements. This feature of the LGI design may allow the device operate under ambient air pressure eliminating vacuum package.

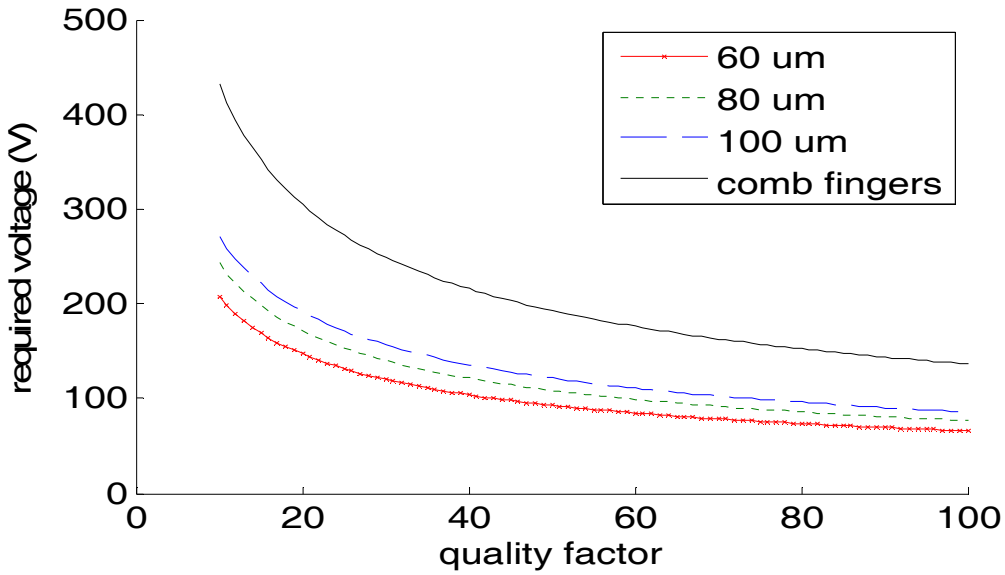

Figure 4.3 – Required voltage levels for operation in resonance for ±500 µm deflection for low quality factors

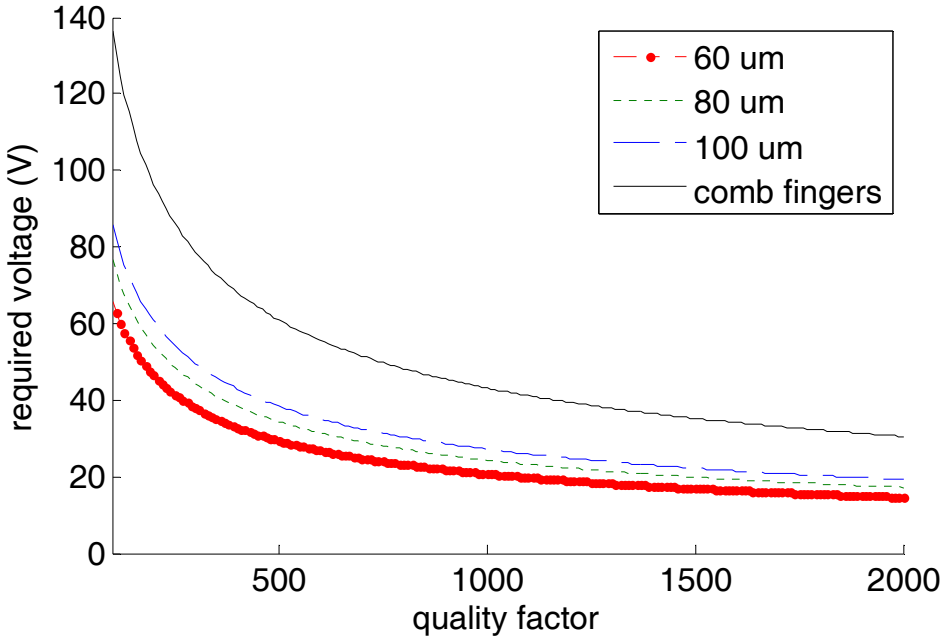

Figure 4.4 – Required voltage levels for operation in resonance for ±500 µm deflection for high quality factors

4.3 Frequency response and start stability voltage

Theoretical frequency response and required starting voltage of the device is extracted by solving equation of motion of the device recursively. Ignoring the other resonance modes the equation of motion for out of plane mode can be written as in (4.9) [26].

$$F_{electrostatic}(z,t) = I_{effective}\frac{d^2z}{dt^2} + b\frac{dz}{dt} + kz \tag{4.9}$$

where $F_{electrostatic}$ is the applied electrostatic force, $I_{effective}$ is effective inertial mass, b is the damping constant, k is the mechanical stiffness, and z is the mechanical displacement. For the applied voltage of V, the electrostatic force can be calculated using the formula (4.10).

$$F_{electrostatic}(z,t) = \frac{1}{2}\frac{dC}{dz}V^2 \tag{4.10}$$

The capacitance change due to displacement is found using ANSYS^{TM} CMATRIX macro. Then, more than one Gaussian functions are superposed to fit into the results obtained from FEM (Figure 4.5). The fit functions are used to calculate electrostatic force and transient response of the system is simulated by solving (4.9) at MATLAB^{TM}. The frequency response of the system is simulated by sweeping the input frequency forward and backward for a quality factor of 50 (Figure 4.6).

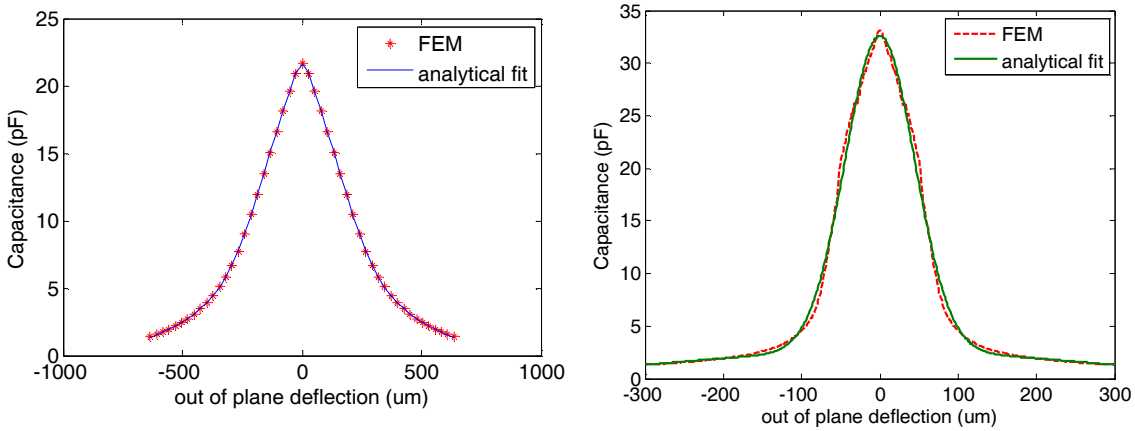

Figure 4.5 – FEM results for capacitance change with respect to out of plane deflection for (Left) comb fingers around pantographs, and (Right) grating fingers with 100µm grating period

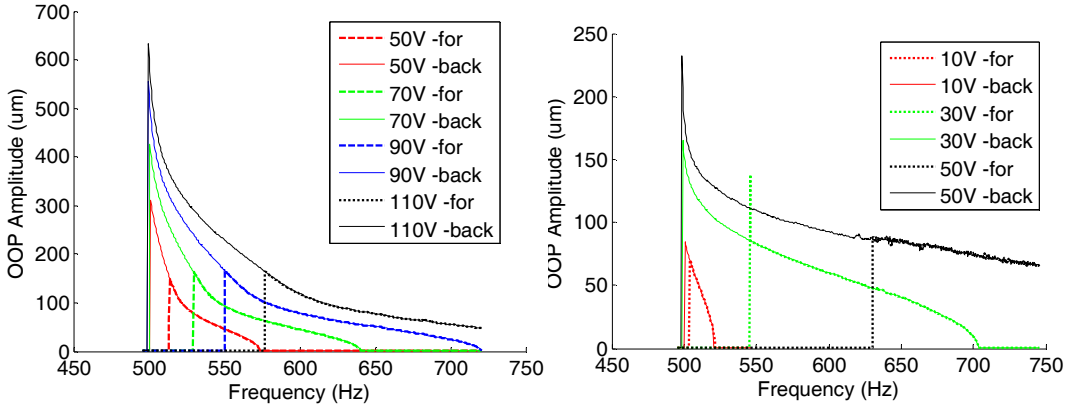

Figure 4.6 – Frequency response of the system using (Left) comb fingers and (Right) grating fingers with 100 µm grating period for sinusoidal excitation. Dotted lines show forward frequency sweep and lines show backward sweep.

As seen in Figure 4.6 the device shows hysteretic frequency response. This kind of behavior is widely examined in [27]-[29]. To start such systems a threshold input voltage level is required. Jump frequencies for forward and backward frequency sweeps are recorded for various voltage levels and start voltage stability curves are obtained as in

Figure 4.7 for a quality factor of 50. The results show that the system requires quite low input voltage to start.

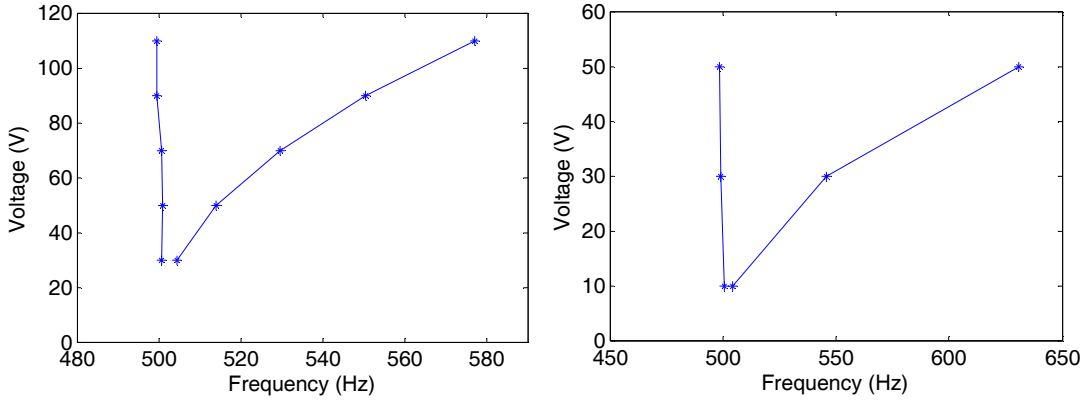

Figure 4.7 – Voltage stability curves (Left) comb fingers and (Right) grating fingers assuming Q=50

4.4 Pull-in voltage

The grating fingers have large aspect ratio. This may cause easy pull-in of the fingers and prevent them being used as a comb drive source. The pull-in voltages are analyzed for each finger type of different grating periods (Table 4.2). Here, the worse scenario is modeled by putting only one finger at one side of another finger, which is completely asymmetric (Figure 4.8). The ANSYS^{TM} FEM results of pull in voltages for different grating periods are as follows:

Grating period	Worse scenario pull-in voltage
30µm	60V
50µm	64V
60µm	85V
80µm	140V
100µm	195V
130µm	290V

Table 4.2 – Pull in voltages for various grating fingers

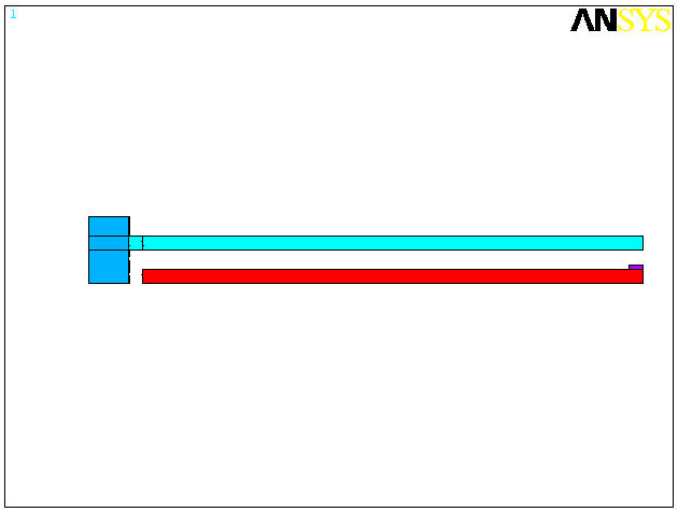

Figure 4.8 – Pull in model for grating fingers. The dimensions are as indicated in Section 4.2.

Because of the pull-in risk at the grating fingers, they are electrically isolated form comb fingers on the pantograph (Figure 4.1). Hence, they can be operated at a lower voltage level if needed.

Chapter 5

5 CONCLUSIONS

A MEMS based advanced Lamellar Grating Interferometer for FTS applications is designed and optimized, and currently being fabricated. The project, funded by FP7 Project titled MEMFIS, aims at developing the world's smallest FTS device that operate in the 2.5um-16um wavelength range with <10cm^{-1} spectral resolution. The MEMFIS project has two primary approaches; one is the LGI approach pursued in this thesis and the other is the Michelson interferometer based approach pursued by Fraunhofer IPMS. The LGI approach compared to the Michelson based approach provides unique and important advantages such as elimination of extra mirrors and beam splitters, compactness, lower-cost, and also possibly the elimination of the vacuum package.

FEM simulations show that the device is able to make ±500 μm out of plane translation with 2 mm by 5 mm clear aperture and 300 nm peak to peak dynamic deformation on grating fingers. Therefore, 10 cm^{-1} spectral resolution will be possible theoretically. A MATLAB^{TM} routine is written for optical simulations based on scalar diffraction theory. Spectral resolution and light efficiency of the device are optimized for the wavelength interval from 2.5 μm to 16 μm with the help of the routine.

The electro-mechanical simulations indicate that multi purpose grating fingers can increase the ease of the motion under ambient air pressure. This is important for removing the vacuum chamber and extra windows needed for the chamber. Therefore, the cost of the system can be reduced while the light efficiency can be increased by operation in ambient air pressure.

BIBLIOGRAPHY

[1] K. Nakamoto, “Infrared and Raman Spectra of Inorganic and Coordination Compounds”, John Wiley and Sons, New York, 1997.

[2] S. Duckett, B. Gilbert, “Foundations of Spectroscopy”, Oxford University Press, West Sussex , 2000.

[3] P. Hendra, C. Jones, G. Warnes, “Fourier Transform Raman Spectroscopy”, Ellis Horwood, West Sussex, 1991.

[4] B. H. Stuart, “Infrared Spectroscopy: Fundamentals and Applications”, John Wiley and Sons, New York, 2004.

[5] V. Saptari, “Fourier Transform Spectroscopy Instrumentation Engineering”, SPIE, Bellingham, 2004.

[6] J. Strong and G. A. Vanasse, “Lamellar grating far-infrared interferometer”, J. Opt. Soc. Am. Vol. 50, Issue 2, p.113, 1960.

[7] J. Strong, “Concepts of Classical Optics”, W. H. Freeman and Company, San Fransisco, 1958.

[8] R. J. Bell, “Introductory Fourier Transform Spectroscopy”, Academic Pr., New York, 1972.

[9] R. C. M. Learner, A. P. Thorne, I. Wynne-Jones, J. W. Brault, and M. C. Abrams. “Phase correction of emission line fourier transform spectra”. J. Opt. Soc. Am. A, Vol. 12, Issue 10, p.2165-2171, 1995.

[10] T. P. Sheahen. “Chirped fourier spectroscopy. 1: Dynamic range improvement and phase correction”, Appl. Opt., Vol. 13, Issue 12, p. 2907-2912, 1974.

[11] T. P. Sheahen and T. O. McCanney. “Phase discrepancies in asymmetric interferograms and application to nonlinearities in Fourier spectroscopy”, J. Opt. Soc. Am., Vol. 65, Issue 7, p. 825-828, 1975.

[12] A. S. Zachor, “Drive nonlinearities: their efects in Fourier spectroscopy”, Appl. Opt., Vol. 16, Issue 5, p. 1412-1424, 1977.

[13] P. Raspollini, P. Ade, B. Carli, and M. Ridol, “Correction of instrument line-shape distortions in Fourier transform spectroscopy”, Appl. Opt., Vol. 37, Issue 17, p. 3697-3704, 1998.

[14] O. Manzardo, “Micro sized Fourier spectrometers”, Ph. D. thesis, 2002.

[15] O. Manzardo, R. Michaely, F. Schadelin, W. Noell, T. Overstoltz, N. F. de Rooij, H. P. Herzig, “Miniature lamellar grating interferometer based on silicon technology”, Optics Letters, Vol. 29, p. 1437-1439, 2004.

[16] http://www.arcoptix.com

[17] F. Lee, G. Zhou, H. Yu, F.S. Chau, “A MEMS-based resonant-scanning lamellar grating Fourier transform micro-spectrometer with laser reference system”, Sensors and Actuators A: Physical, Vol. 149, p. 221-228, 2009

[18] C. Ataman, H. Urey, A.Wolter, “A Fourier transform spectrometer using resonant vertical comb actuators”, Journal of Micromechanics and Microengineering, Vol. 16, p. 2517–2523, 2006.

[19] C. Ataman, “MEMS scanners for spectroscopy and laser scanning systems”, Ph. D. thesis, 2008.

[20] H. Urey, C. Ataman, European Patent 1677086, Issued: 2006.

[21] http://www.memfis-project.eu/

[22] A. Tortschanoff, A. Kenda, M. Kraft, T. Sandner, H. Schenk, W. Scherf, “Improved MOEMS based ultra rapid Fourier transform infrared spectrometer”, Proc. of SPIE, Vol. 7319, 73190I , 2009

[23] T. Sandner, C. Drabe, H. Schenk, A. Kenda, W. Scherf “Translatory MEMS actuators for optical path length modulation in miniaturized Fourier-transform infrared spectrometers”, J. Micro/Nanolith. MEMS MOEMS, Vol. 7 (2), 021006, 2008

[24] T. Sandner, A. Kenda, C. Drabe, H. Schenk, W. Scherf, “Miniaturized FTIR-spectrometer based on optical MEMS translatory actuator”, Proc. of SPIE, Vol. 6466, 646602, 2007.

[25] J.W. Goodman, “Introduction to Fourier Optics”, Roberts & Company Publishers, Greenwood Village, 2005.

[26] S.D. Senturia, “Microsystem Design”, Springer Science and Business Media, New York, 2001

[27] C. Ataman, H. Urey, “Nonlinear frequency response of comb drive microscanners,” Proc. SPIE of MOEMS Display and Imaging Sytems II, vol. 5348, pp. 166- 174, 2004.

[28] H. Schenk, P. Dürr, T. Haase, D. Kunze, U. Sobe, H. Lakner, H, Kück, “Large deflection micromechanical scanning mirrors for linear scans and pattern generation,” IEEE Journal Of Selected Topics In Quantum Electronics, vol. 6, pp. 715- 722, 2000.

[29] C. Ataman, H. Urey, “Modeling and characterization of comb-actuated resonant microscanners,” Journal of Micromechanics and Microengineering, vol. 16, pp. 9-16, 2006.